Diplomarbeit

Simulationsgetriebener Entwicklungs- und Optimierungsansatz für Polymer-Spritzgusskomponenten mit nichtlinearem Kontakt- und Materialverhalten

ausgeführt zum Zwecke der Erlangung des akademischen Grades eines
Diplom-Ingenieurs

Diploma Thesis

Simulation-driven development and optimisation approach for polymer injection moulded components with non-linear contact and material behaviour

submitted in satisfaction of the requirements for the degree of
Diplom-Ingenieur
of the TU Vienna, Faculty of Mechanical Engineering
handed in at the Vienna University of Technology, Faculty of Mechanical Engineering

by

Sebastian Alfons Erich Rigger, BSc

Matr.Nr.: 01127847

under the supervision of

Ao.Univ.Prof. Dipl.-Ing. Dr.techn. **Manfred Grafinger**

Institute of Engineering Design and Product Development
Research Division Mechanical Engineering Informatics and Virtual Product Development
Vienna University of Technology
Lehárgasse 6, Obj. 7, 1060 Vienna, Austria

Vienna, on the 27. November 2023 _____

Affidavit

I herewith declare on oath that I wrote the present thesis without the help of third persons and without using any other sources and means listed herein. I further declare that I observed the guidelines for scientific work in the quotation of all unprinted sources, printed literature and phrases and concepts taken either word for word or according to meaning from the Internet and that I referenced all sources accordingly.

This thesis has not been submitted as an exam paper of identical or similar form, either in Austria or abroad and corresponds to the paper graded by the assessors. I acknowledge that the submitted work will be checked by electronic technical means (plagiarism detection software) that are suitable and in accordance with the current state of the art. On the one hand, this ensures that the high quality specifications within the framework of the applicable rules for ensuring good scientific practice "Code of Conduct" at the Vienna University of Technology were adhered to in the preparation of the submitted work. On the other hand, a comparison with other student theses avoids infringements of my personal copyright.

City and date _____ *Signature* _____

Acknowledgements

I express my deepest appreciation to my parents, Renate and Alfons, for their unwavering support throughout my academic journey. My heartfelt thanks to my sisters, Hannah and Theresa, for the lighthearted camaraderie that offered a welcome break from the academic challenges.

Special acknowledgement goes to Stefan, who has always been an invaluable conversation partner and whose expertise in mathematics and dedicated assistance with algorithm optimisation in Julia were instrumental in the success of this work.

I am grateful for the support of my former colleagues at V-Research and Thomas and Emanuel, whose belief in a positive outcome and attentive listening eased the challenges of the project.

Dr. Jörgen Bergström deserves special mention for his patience in answering my queries about material models and his proactive efforts in testing and validating my model.

Lastly, my sincere gratitude to the specialist group for High Performance Computing/data-LAB at *TU.it*. The stable working environment provided within the Little Big Data cluster, and Dieter Kvasnicka's extensive assistance in setting up *Ansys* on the cluster, were invaluable for running the resource-intensive simulations in the final phases of the project.

Kurzfassung

Die frühe Phase der Produktentwicklung hat erheblichen Einfluss auf die Markteinführungszeit und die Kosten eines Produkts. Ingenieure suchen nach Möglichkeiten, diesen Prozess zu beschleunigen und gleichzeitig die Qualität zu verbessern, was zur weit verbreiteten Anwendung von Computersimulationen geführt hat. In dieser Arbeit wird der Einsatz von strukturmechanischen Simulationen zur Unterstützung von Designentscheidungen bei der Entwicklung und Produktion von spritzgegossenen Beleuchtungskomponenten aufgezeigt und bewertet. Diese Bauteile müssen strenge Prüfungen gemäß internationaler Normen bestehen, wobei ein Versagen kostspielige Anpassungen an den Spritzgusswerkzeugen sowie die Wiederholung des Testablaufs erfordert.

Die *Methode der Dimensionsreduktion* wird angewandt, um das *3D*-Problem mathematisch zu übersetzen und die numerische Optimierung zu erleichtern. Konkret wird eine greifbare und handhabbare Methode zur Optimierung einer Zugentlastungskomponente eines *LED*-Treibergehäuses aufgezeigt, wobei notwendige begleitende Aufgaben wie die Kalibrierung des Materialmodells und die Bestimmung des Reibungskoeffizienten behandelt werden. Die Ergebnisse ermöglichen eine qualitative Bewertung und zeigen eine leichte Verbesserung des ursprünglichen Designs, indem die Widerstandsfähigkeit gegen Kabelauszugskräfte verbessert wird, während gleichzeitig die Belastungen der Komponenten reduziert werden. Diese Erkenntnisse bilden eine Grundlage für weitere, vertiefte Forschung und bieten Einblicke in das Potenzial für die vollständige Simulation standardisierter Prüfroutinen. Die Auswirkungen dieser Arbeit erstrecken sich auf potenzielle Kosteneinsparungen und Effizienzsteigerungen in den Produktentwicklungsprozessen.

Abstract

The early phase of product development significantly influences the time-to-market and cost of a product. Engineers seek ways to expedite this process while enhancing quality, leading to the widespread adoption of computer simulations. In this work the use of structural mechanics simulations to support design decisions in development and production of injection moulded lighting components is highlighted and evaluated. These components must undergo rigorous testing according to international standards, and any failure necessitates costly adjustments to injection moulding tools and a repetition of the test routine.

The *Method of Dimensionality Reduction* is applied to mathematically translate the *3D* problem, facilitating numerical optimisation. Specifically, a tangible and tractable way of optimising a *LED* strain relief component is illustrated, addressing necessary accompanying tasks such as material model calibration and the determination of the coefficient of friction. The results enable a qualitative evaluation, showing a slight improvement in the initial design, enhancing its ability to withstand cable pull-out forces while reducing component stresses. These findings provide a foundation for further, more in-depth research and offer insights into the potential for fully simulating standardized test routines. The implications of this work extend to potential cost savings and efficiency gains in product development processes.

Contents

List of Figures

List of Tables

Acronyms

1D one dimensional

2D two dimensional

3D three dimensional

APDL Ansys Parametric Design Language

CAD Computer Aided Design

CAE Computer Aided Engineering

CAM Computer Aided Manufacturing

CAO Computer Aided Optimisation

CLSM confocal laser scanning microscope

CNC Computerized Numerical Control

COF coefficient of friction

DIY do it yourself

DOE design of experiments

DOF degrees of freedom

FEA finite element analysis

FEM Finite Element Method

LED Light-emitting diode

MDR Method of Dimensionality Reduction

PC polycarbonate

PN Parallel Network

PVC polyvinyl chloride

PVC-P plasticised polyvinyl chloride

SKO Soft Kill Option

TN-Model Three Network Model

TNM Three Network Model

TO Topology Optimisation

UTS ultimate tensile strength

Chapter 1

Introduction

The application of computer aided technologies (*CAx*) in product development and manufacturing is an established practice and has been so for many years. Using methods like computer aided design, manufacturing or engineering (*CAD/CAM/CAE*) increases the development efficiency, product quality and reduces the probability of errors throughout the life cycle [1]. Modelling a product in *3D* helps visualising its design and dimensions before actually manufacturing it. The same model can then be used for simulations, e.g. structural mechanics analysis using the finite element method (*FEM*) [2], for manufacturing purposes, e.g. virtual collision checking of *CNC* milling tools, or as the first step towards a *Digital Twin*, a full digital representation of a product along its life cycle [3]. In recent years *CAE* grew immensely in popularity and found a wide range of applications in industry. Research was conducted on how to introduce this technology into product development, e.g. [4–6], and the terms *Simulation Based Design* and *Simulation Based Engineering* were coined. Simulations proved valuable not only during the initial product development, but also for optimisation purposes during development iterations.

1.1 Motivation

The project at hand focuses on highlighting the value of structural mechanics simulations as a development supporting role at the industrial partner, a company developing and producing lighting components, and its findings should act as a proof of concept. Initially thermal simulations were already used in the company, e.g. for analysing the heat dissipation in *LED* drivers, but there was no prior experience regarding structural mechanics simulations. As a use case the design of a cable strain relief module in *LED* driver housings was identified, see Fig. 1.1. This module is intended to fix the cable in place and prevent it from being pulled out of the electrical contact inside the housing. It protects the cable from stress-related damage, prevents breakage

of conductors and connectors and ensures full functionality of the electronics. Its function is realised through small indenting bodies, one can imagine these as tiny teeth, located on the clamp and housing, which penetrate the cable sheathing when the clamp is pressed into position. Fig. 1.1a shows the real *LED* driver and identifies its components and Fig. 1.1b visualises its virtual representation as a *3D CAD* model with the relevant components' type of material, which will be of further interest in the following chapters of this work. One can see, that the electrical components of the driver were already omitted during the virtualisation, as they are obsolete for the further steps since they don't have any influence on the strain relief functionality.

In order to be declared or certified as "safe to use", these components must be tested and checked whether they comply with the applicable standards. The OVE EN 60598-1 [7] is one of those standards and it details the general requirements and associated tests of luminaires, including the mechanics of the structure of the components housings which includes the strain relief module. For this specific module it states:

- **test setup:** the cable conductors are lightly tightened in their respective places of the terminals, i.e. the electrical contact, the strain relief functionality is applied, i.e. the clamp is to be pressed into the cable, and a mark is made on the cable at a distance of approximately 20 mm of the strain relief.
- **test procedure:** the cable is subjected to 25 consecutive pulls, each time for 1 s, whereas the amount of force applied is dependent of the total nominal cross-sectional area of all conductors of the cable and lies between 30–120 N.
- **test outcomes:** To pass the test, the mark isn't allowed to be displaced by more than 2 mm, the conductors shouldn't have moved in the terminals and the cable shouldn't be damaged during and after the tests. If the terminals are suspected to partly work as an anchorage due to an insufficiency of the strain relief, the test has to be repeated with opened terminals.

The total nominal cross-sectional area of conductors depends on the cable type, which is introduced and explained in section 2.3.

If changes are made to the component, these tests must be carried out again. The polycarbonate (*PC*) components are manufactured in an injection moulding process [8], which is economically efficient if used for a high number of parts but the tools or moulds to produce the

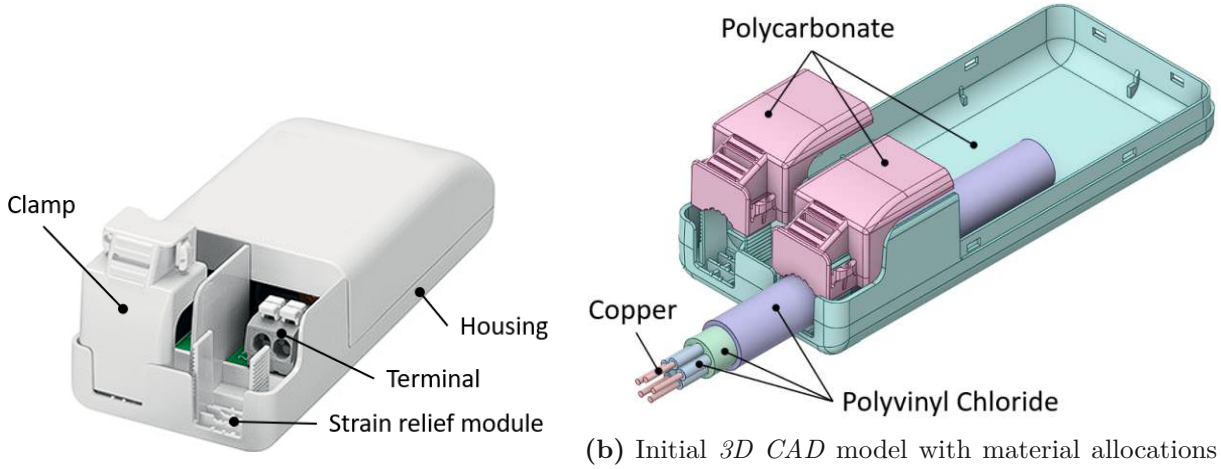

(a) *LED* driver as sold by the industrial partner

(b) Initial *3D CAD* model with material allocations and without housing cover

Fig. 1.1: Side by side visualisation of a real *LED* driver and its *3D CAD* representation

parts are not only expensive but also time intensive to manufacture. If a standard test fails, the strain relief design needs to be adapted and new tools must be ordered which potentially causes severe project delays and results in additional costs. One could argue, that carrying out the standard tests with alternatively manufactured prototypes, e.g. milled, could be a viable intermediate step to check whether the test can be carried out successfully. Unfortunately but not surprisingly, the type of manufacturing proved to have a significant influence on the test results and no reliable conclusions could be drawn from this approach. The problem the engineers at the industrial partner are facing, is being bottle necked by the mandatory testing of the mechanical requirements of the *LED* driver housings' strain relief module and the necessity of manufacturing the test specimen with expensive injection moulds. The use of simulations is intended to remedy the situation and act as a tool to accelerate development by eliminating the need for multiple adjustment iterations, leading to a single ordered injection mould.

For the translation of the standardised test into a simulation concept, the actions are divided into two steps, we will call them load steps:

Load Step 1 Activate the strain relief function, i.e. press the clamp into the cable.

Load Step 2 Apply a pull-out force to the cable at a distance of about 20 mm of the strain relief.

The second load step can then be repeated 25 times or, neglecting any elastodynamic reaction effects of the cable sheath material for simplification, the resulting displacement after

the first pull is multiplied by 25 to obtain the total displacement. Later we will see that this load step is further simplified to reduce the vast resource consumption of the simulation model.

The aim of this work is to define a possible structural mechanics optimisation process to successfully value design choices and make qualitative statements in regards to the strain relief module of a *LED* driver component. For this purpose several experiments were conducted in order to calibrate a viscoplastic material model and a stable simulation model is built. On the following pages it is shown that eventually *FEAs* and analytical calculations based on the *Method of Dimensionality Reduction* (*MDR*) in contact mechanics were used in combination to obtain meaningful results. In order to limit the complexity, an optimal design of the indenting bodies in the strain relief module is sought, while the basic geometry of the components is retained for the time being.

1.2 State of the Art

Simulations are widely used for structural optimisation procedures in industry and research, where locations of high stress concentrations are, for example, identified with finite element analyses (*FEAs*). There is a large body of literature on the application of structural optimisation to systems with linear material and contact behaviour and isolated simple geometries that can be easily translated mathematically, e.g. two dimensional problems. Mechanically loading a truss or beam is a classical problem in topology optimisation (*TO*) [9] and popular in research, where different methods and their overall efficiency are compared [10–12]. *FEM* is also applied in the field of polymer science, e.g. for analyses of o-ring sealing mechanisms [13] or predictions of the service life of sealing elements [14], but the literature on multibody systems with high penetrations and deformations at the interface of the contacting bodies, as expected for the problem at hand, seems to be scarce. Approximation concepts can be applied to multibody systems to reduce complexity where a direct coupling of analysis and mathematical programming algorithms is hindered or not possible [15]. Multibody problems can be solved using multilevel optimisation methods, i.e. through iteration between multibody *3D*, cross-sectional *2D* and *1D* spatial beam models, e.g. for a wind turbine rotor blade optimisation [16], or through dimensional reduction in general [17].

MDR is a well-established technique in the field of contact mechanics, see [18], but to the best of the author's knowledge has not yet been applied to real-life engineering problems. In this

sense, the approach taken in this work, which aims to integrate *MDR* into product optimisation, seems to be new.

Chapter 2

Fundamentals & Methodology

The purpose of this chapter is to familiarise the reader with the basics of the methods used in this thesis. Although some basic principles of fundamental engineering methods are included, most of the theory in this work is aimed at those with background or prior knowledge in specific engineering research areas, including but not limited to finite element analysis, material science and numerical optimisation.

2.1 Finite Element Analysis

Numerical solution techniques have been developed since the early 20th century but until the utilisation of modern digital computers they only had limited usability. The significance of numerical methods rose with the deployment of powerful computer systems to a point that in recent history, the growing availability of more affordable computing resources led to the application of computer-aided methods for day-to-day operations in many areas of engineering [1] – the finite element method is one of those.

The basic principle behind *FEM* involves the partitioning of a component into smaller finite geometrical sections, the "*finite elements*". These hypothetical elements are linked to the physical component via the coordinates of their corners or nodes and when all elements are considered together, they describe the shape of the component. With the definition of boundary conditions such as bearings, supports, etc. and the application of a load, the input of the problem is completed. During the calculation of the static state of equilibrium, done by solving a set of differential equations by the *FEM* program, the balance of the internal nodal forces caused by

stresses within the body and the external nodal forces due to loads is determined [19]. For linear problems, the equation to be solved is basically *Hooke's Law* in matrix form:

$$\mathbf{F} = \mathbf{K} \cdot \mathbf{u} \tag{2.1}$$

Here $\mathbf{F}$ is the force tensor, $\mathbf{K}$ the stiffness matrix and $\mathbf{u}$ the displacement tensor. By inverting the stiffness matrix the nodal displacements can be computed directly:

$$\mathbf{u} = \mathbf{K}^{-1} \cdot \mathbf{F} \tag{2.2}$$

For linear problems the stiffness matrix is constant and a solution is obtained in a single step. For non-linear problems the stiffness matrix is not constant and a sequence of linearised problems has to be solved.

In present times, applying *FEM* is commonly done with commercially available software tools. Open-source or freeware software solutions, such as *OpenFOAM*, can be used for highly specified cases or trivial problems, but often lack the functional scope and/or user-friendliness of their fee-based competitors provided by the established simulation software vendors, e.g. Ansys, Inc. or Altair Engineering Inc.. For the problem at hand the software suite by Ansys, Inc. was used for the simulations and most of the associated additional preprocessing tasks. This includes *Ansys Workbench* for defining material models and creating systems containing several individual or interconnected simulations, *SpaceClaim* as an integrated *CAD* tool for adapting the *3D CAD* model and *Mechanical* for performing the actual simulation. For the creation of advanced material models *MCalibration*[1] was used, as their fitting is not supported in *Ansys Workbench*.

The typical workflow of a *FEM* analysis can be split into several main tasks [1]:

1. Clarification of the research question
2. Simulation model design
3. Creation of a *FEM* model (Preprocessing)
4. Calculation with *FEM* solver (Processing)
5. Visualisation of results (Postprocessing)

[1] https://polymerfem.com/mcalibration/

6. Interpretation of results

While we already defined the scope of this work in the previous chapter, we shall have a detailed look on the other mentioned main tasks, leaving out *Interpretation of results*, since it is self explanatory. The preprocessing step is particularly noteworthy, as this is where most of the expected workload lies when carrying out an analysis. For complex models convergence is usually not achieved after the first calculation run, so several adjustments have to be made, e.g. additional iterations of the preprocessing phase must be carried out. Fig. 2.1 shows the typical sequence of an *FEA*.

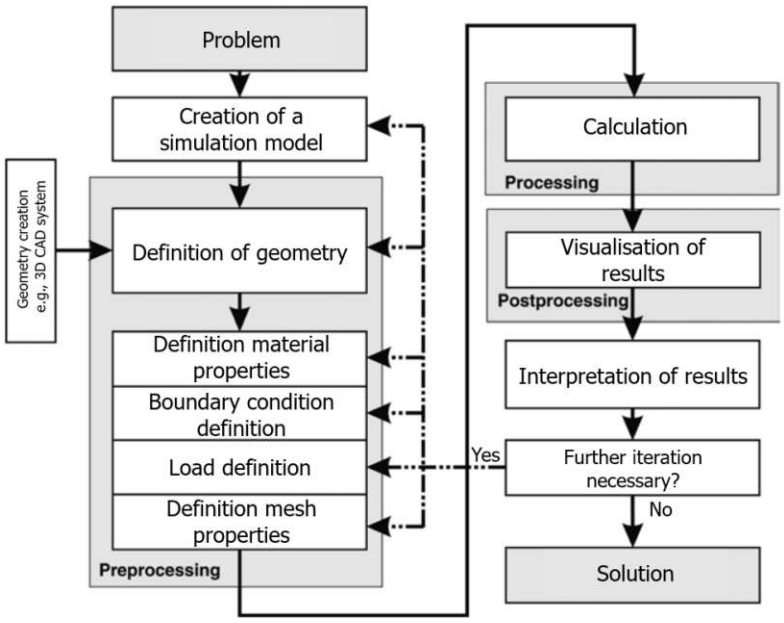

Fig. 2.1: Task sequence of an *FEM* analysis. Source: [1]

2.1.1 Simulation Model Design

Before conducting a *FEM* simulation, one starts abstracting the problem at hand including applying idealisations and simplifications [1], and specifying the outline of the intended analysis, i.e. definition of an overall simulation concept – e.g. Its type, meaning *2D* or *3D*, implicit or explicit, its goal and the way how it will be accomplished. This can be done as a thought model by answering general questions that accompany any analysis [1], such as:

What problem should be solved? What questions are supposed to be answered? What preparations must be made, e.g. calculations, comparison of allowable values of physical properties?

Is the problem solvable through mathematical models and *FEM*? Is the required data available? How can one validate the results?

There are many different ways of approaching an analysis and a method which was easily and successfully applied before on a different model may not yield the expected outcome in another situation. The chosen simulation concept directly influences the preprocessing phase. It is generally a good idea to start as simple as possible and gradually increase the complexity.

Several *2D* and *3D* simulations were carried out as part of this work. While *2D* simulations are a manageable and resource-efficient way to validate small assumptions or compare design choices, *3D* analyses are generally significantly more time-consuming and should be planned carefully .

2.1.2 Preprocessing

One can further break down the preprocessing phase into several subtasks as seen in Fig. 2.1.

2.1.2.1 Definition of Component Geometry

The geometry was initially provided as a *3D CAD* model by the industrial project partner. Generally, one of the first steps in preprocessing is to simplify the model. Typical simplification tasks include:

- detaching a region of detail for closer examination,
- reduction of the level of detail,
- utilising (local) symmetries to reduce mesh element count,
- applying fillets to sharp corners and edges, since they lead to stress singularities.

Due to manufacturing tolerances, the cables generally have a large tolerance range with regard to their diameter. In order to illustrate the flexibility and robustness of the simulation models, simulations were carried out with the respective extreme values, i.e. minimum and maximum diameter, which ultimately were successful and did not show any significant deviations in the results.

2.1.2.2 Material Model Design

Material models characterise the relation between external load and the resulting internal stress distribution. One should be aware of the materials of the components and their physical properties

to properly calibrate a material model and reproduce realistic behaviour in the simulation. To accomplish this task, one either has sufficient material-describing data available in advance – either through access to a material databases or taken from literature – or must extrapolate it through experiments. For the problem at hand the involved components are predominantly polymers. Fig. 1.1b shows the system and the materials which they consist of.

Describing the viscoplastic nature of thermosets, such as *plasticised polyvinyl chloride* (*PVC-P*), necessitates a different approach than the modelling of linear elastic or plastic material behaviour of hard materials such as metal and/or *polycarbonate* (*PC*). Fig. 2.2 visualizes the typical stress-strain responses during tensile loading of different materials. The literature offers many different material models for rubber like materials. Each one has its justification for existence and is a good choice, at least for the specific use case for which it was developed. The author found the book *Mechanics of Solid Polymers* by Dr. Jörgen Bergström[2] to contain an excellent collection of material models and in-depth knowledge about polymers in general. Of the mentioned materials, the behaviour of copper would correspond to curve *c*, *PC* to curve *g* and *PVC-P* to curve *h* in Fig. 2.2. Taking the applied load and the induced stress to be expected with it into account, we dive deeper into the methodology and start off with the material with the simplest elastodynamic behaviour, copper.

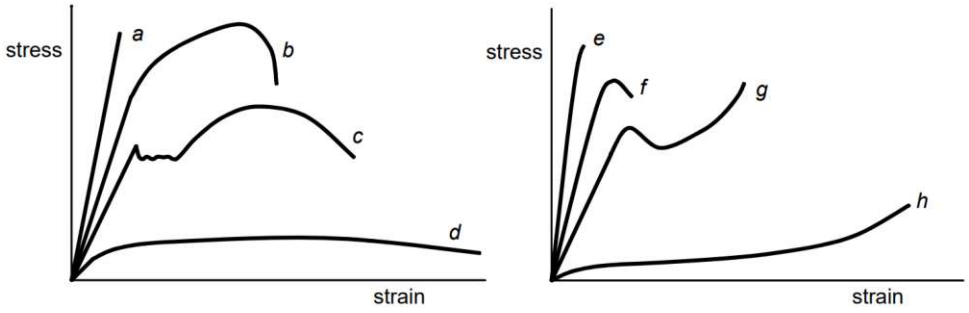

Fig. 2.2: "Schematic depictions of typical engineering stress-strain tensile curves for (*a*) ceramic and glass materials, (*b*-*d*) metals, (*e*-*h*) polymers." Source: [20]

Copper

The conductors in the cable – either in the form of solid or stranded wire – are made of copper. First result evaluations unsurprisingly showed, that the stress induced through our load cases is restricted to regions way below the yield strength of the material. This means that the material is showing a linear relationship between stress and strain and its isotropic elasticity can be fully reproduced in simulation knowing its *Young's Modulus* and *Poisson's Ratio*, which are generally

[2]founder of PolymerFEM, prolific material scientist and developer of the *Bergstrom-Boyce Model*

known and do not need to be determined – at least for the solid wire.

The division of the cross-sectional area of a solid wire into several smaller strands introduces orthotropic flexibility to the cable model, i.e. the material properties in the axial direction remain constant, while the flexural rigidity of the system decreases in any orthogonal direction to it. One can simply observe this through do-it-yourself (*DIY*) cable bending experiments at home – a solid wire is stiff and difficult to bend, while a stranded wire is flexible. The model has to be adapted for the special case of the stranded wire, so an orthotropic elasticity model was defined and tested, reducing the flexural rigidity by a certain factor according to the literature [21, 22]. Although the results look promising, they were not validated as the focus of the work was mainly on the optimisation process, which for simplicity was studied using solid wire models.

Polycarbonate

To simulate the behaviour of the polycarbonate MAKROLON ® 2467, the *Multilinear Isotropic Hardening Model*[3] has been chosen. Although much of the previously mentioned properties of copper also apply to the polycarbonate, as it only experiences elastic deformations under the loads we apply, the induced stresses are much closer to the yield strength of the material and this model allows for larger strains. The material data needed to define the model is openly accessible and provided on the world wide web by the manufacturer COVESTRO AG itself [23].

Plasticised Polyvinyl Chloride

The cable sheath and the wire insulators of the system are made of *PVC-P*, which can be described as rubberlike in behaviour. As a simplification, it was assumed that these components are made of exactly the same type of *PVC-P*. *PVC* is a thermoplastic and is produced in rigid or flexible form, which is achieved through addition of plasticisers to the raw material before manufacturing. Other typical additives which are used for electrical cables are flame retardants, UV stabilisers, fillers, etc. The choice of additives leads to a variety of possible material compositions, and as a result, *PVCs* from different manufacturers that initially appear similar can be fundamentally different in terms of their properties. knowing this, material data deriving experiments must be carried out on the original material.

As far as virtual representation is concerned, there are many ways to simulate rubberlike materials. The already mentioned plasticity model can be used, although for high strains and

[3] As named in *Ansys Workbench*, also called *Isotropic Hardening* or *plasticity theory*

non-linear viscoplastic responses – which can be expected of *PVC-P* – poor predictions are likely, particularly during cyclic loading [24]. For materials with high strains, hyperelastic material models are widely used and appreciated for their ease of use, e.g. the *Neo-Hooke Model*. They are considered to be a good starting point in modelling high deformable materials such as elastomers. Their typical characteristics include no residual strains after unloading, no hysteresis while cyclic loading, no creep, no relaxation, etc. In the absence of material samples of sufficient quality for experiments, the *Neo-Hooke Model* was used in the present analysis systems over a longer period of time. Later on when material specimen were provided, the *Three Network Model* (*TNM*) was calibrated, which is a viscoplasticity model that was specifically developed for thermoplastic materials. These sort of models are supposedly unrivalled in terms of accuracy and complexity and are able to predict non-linear, time- and temperature-dependent behaviour, but require extensive experimental data for proper calibration [24].

As mentioned before, *MCalibration* was ultimately used to calibrate the *TN-Model*. For an initial evaluation of the magnitude of the prediction errors the software calculates the *normalized mean absolute value* (*NMAD*) [24]. To validate the material models, the experiments performed are customarily replicated in the simulation and the results are compared.

2.1.2.3 Boundary Condition and Load Definition

Since the simulation was carried out with *Ansys Mechanical*, this chapter deals with the application-specific mode of operation and function naming. If not further specified, program specific knowledge was taken from the *Ansys Mechanical User's Guide* [25].

Boundary conditions and loads should be reproduced as close to reality as possible, but are commonly idealised, e.g. locked degrees of freedom (*DOF*) due to forbidden rigid body movement in static simulations despite the fact that the real components can perform rigid body movements [1]. If planar symmetries of a system are exploited, movement or deformation in the normal direction, relative to the selected face, has to be prevented. This can either be done with a *displacement* boundary condition or a *frictionless support*, which corresponds to the former if only the displacement in one direction, i.e. the normal direction, is locked. To simulate a firm connection or fixation, the *fixed support* or *displacement* with no free direction is usually used. In a static structural simulation, as performed for the problem at hand, the load will either be applied through the already mentioned *displacement*, e.g. a body is indented into another, or as a *force*, applied on a geometric object, such as a point, edge or face. In general, a force

Scope	
Scoping Method	Geometry Selection
Contact	2 Faces
Target	10 Faces
Contact Bodies	Cable sheath
Target Bodies	Solid
Protected	No
Definition	
Type	Frictional
Friction Coefficient	0,5
Scope Mode	Manual
Behavior	Symmetric
Trim Contact	On
Trim Tolerance	1, mm
Suppressed	No
Advanced	
Formulation	Program Controlled
Small Sliding	Off
Detection Method	Program Controlled
Penetration Tolerance	Program Controlled
Elastic Slip Tolerance	Program Controlled
Normal Stiffness	Program Controlled
Update Stiffness	Each Iteration, Aggressive
Stabilization Damping Factor	0,
Pinball Region	Radius
Pinball Radius	0,5 mm
Time Step Controls	None
Geometric Modification	
Interface Treatment	Adjust to Touch
Contact Geometry Correction	None
Target Geometry Correction	None

Fig. 2.3: Settings for contact definition as seen in *Ansys Mechanical*

driven analysis is the simplest way for load application, while a displacement driven analysis leads to a more robust and stable system. Therefore, choosing a displacement driven approach is favourable [26], especially if convergence problems occur. The user has the choice of either conducting the simulation in a single or in multiple load steps. Though load variations can be defined in a single load step, multiple steps have the advantage that the user can control the analysis settings or boundary conditions more comprehensively for each individual load step. Furthermore, boundary conditions between touching bodies, i.e. faces of bodies which are in contact, including those which will be doing so at any time along the simulation, have to be defined. Setting the appropriate contact definition can prove to be a laborious process, since there are many factors which have to be considered. Each contact has a target and a contact side. While the target side only provides information about the position of individual points, the contact side also provides information about the surface geometry itself. A badly selected

contact pair tends to enable unwanted penetrations. According to [26], the rules of thumb state that the target side should be the one with:

1. the coarser mesh,
2. the larger surface,
3. the less curved or flat surface,
4. the surface with the lower order mesh,
5. the stiffer underlying material.

The basics of the most prominent advanced contact setting options shall be mentioned here, see [26] for a more detailed description. Fig. 2.3 shows the contact settings pane in *Mechanical*. These contain:

Type of contact, including frictionless and frictional contact. As one can expect, the frictional contact introduces an additional parameter, the coefficient of friction (COF) μ, which is dependent of the two surfaces in contact. This type behaves according to the well known friction laws of Amontons[4] and Coulomb[5], which states that the maximum tangential force $|R|$ that can be transferred between two bodies at a planar interface, before sliding occurs, is independent of the area of contact and proportional to the compressive normal force N [27], see Eq. 2.3

$$|R| \leq \mu \cdot N \tag{2.3}$$

Behaviour either defines a contact as *asymmetric*, i.e. one contact pair with a contact and target side, which delivers better performance, or as *symmetric*, which additionally defines the contact a second time, as done for the *asymmetric* option, but with switched contact and target side. This is recommended if the previously mentioned rules of thumb contradict each other for the specific contact pair, but it will consume more computing resources.

Pinball Region enables the user to specify a region in which the program should search for the contact partners. This is necessary if the contacting faces do not touch initially, i.e. there is a gap or penetration, e.g. one contact partner is indented into the other. In such cases the program will not detect the contact without a *pinball region*.

[4] Guillaume Amontons (1663-1705), french physicist
[5] Charles-Augustin de Coulomb (1736-1806), french engineer and physicist

Interface Treatment defines the procedure how a contact pair interface is handled and can improve the contact status if applied properly. If many individual contact regions become active at different time points, initial gaps or penetrations can occur. For better convergence, it is beneficial to cushion these influences with interface options such as *Adjust to touch*, which either closes gaps or removes penetrations and creates an initial stress free state.

2.1.2.4 Definition of Mesh Properties

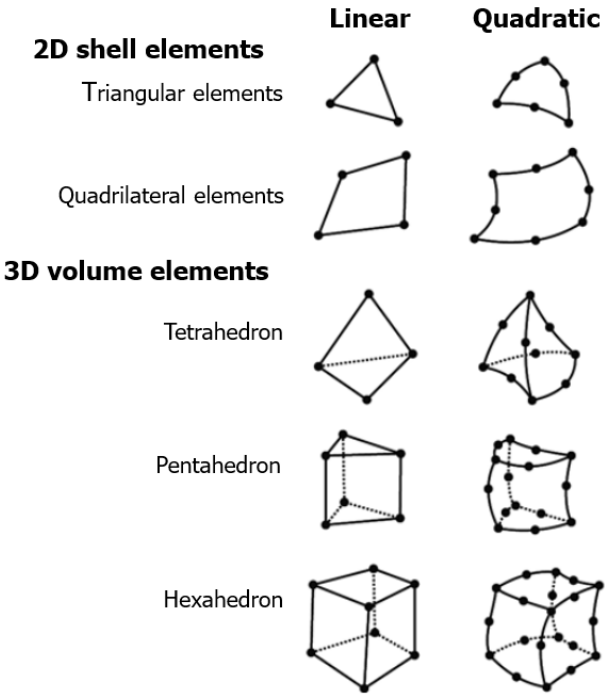

Fig. 2.4: Element types and their node positions in linear or quadratic order. Source: [1]

Although *FEM* software commonly includes an automatic meshing tool, it is often necessary to adjust the generated mesh to fit the load case of the simulation model. The options for meshing are at least as plentiful as the contact definition settings and might be considered a form of art if mastered. If done improperly convergence may never be reached. First of all, the user has the choice between different geometry types of elements – the most regularly used ones are tetrahedra and hexahedra – and linear or quadratic elements, i.e. the element order, which determines whether or not mid nodes are used at edges between element corner nodes. When meshing, one has to keep in mind, that compared to a quadratic order mesh, a mesh consisting of linear element shapes of the same type needs a higher mesh resolution to achieve a comparable accuracy of results, but that quadratic meshes require considerably more computing time with the same number of elements. This is easily comprehensible if one compares the amount of nodes between

a linear and quadratic element of the same geometric type, e.g. a linear hexahedron has 8 nodes while a quadratic one has 20, see Fig. 2.4. If the mesh resolution stays constant, hexahedra are preferable over tetrahedra, since they empirically yield better results [1]. Furthermore, for good mesh quality, it is also important that the elements do not deviate too much from their optimal shape or deform heavily during the analysis. When it comes to complex, specially shaped geometries, tetrahedra are often preferred over hexahedra, as they offer greater flexibility and computational stability with larger element distortions. Ultimately, the engineer must decide how to mesh to keep the computation time as low as possible while achieving satisfactory result quality.

2.1.3 Processing

During the processing phase the software calculates the results and tries to achieve convergence with respect to the internal stress state caused by the external boundary conditions. The outcome of the analysis is heavily influenced by all the prior mentioned steps. As for the program's way of approaching the calculation, without going into much detail, one can modify the analysis settings, e.g. add load steps, define the amount of minimum and maximum *substeps* during a single load step, the *Solver Type*, etc. For non-linear analyses with hyperelastic materials or high deformations, it is important to activate the *Large Deflection* option, which "*(...) will take into account stiffness changes resulting from change in element shape and orientation due to large deflection, large rotation, and large strain.*" [25].

During the processing phase, there aren't many possibilities to influence the outcome of the analysis, but through monitoring the convergence tendency of the system with the help of real time result display options like *Force Convergence*, *Displacement Convergence* or the *Solver Output* itself, which documents the analysis progress in textual form, divergent calculation runs can be identified and aborted at an early stage. The *Contact Tool* is also a handy instrument for monitoring contact regions in real time. The different options to display include, among others, the status of the contact, e.g. if it is indeed closed or still open, the pressure transmitted through the contact zone or the penetration that occurs at a specific contact region.

2.1.4 Post-processing

Post-processing is dominated by two activities – validation and visualisation of results. Almost everybody has already encountered a fancy *FEM* plot. Kept in bright, high contrast colour

schemes, they either show regions of high stress or strain gradients, or something similar, but a result can appear as flamboyant as a peacock during mating season, if it isn't verifiable one should be careful and not succumb to its vacuous play of colours. In an ideal case, one has quantifiable parameters that have been measured in experiments or calculated analytically to compare with the simulation results. For the problem at hand several different experiments have been conducted to validate specific load steps and the final outcome itself, see section 2.3.

Often the results of post-processing are used to define another, more detailed calculation iteration. This can be done several times until the accuracy of the result reaches a satisfactory range.

2.2 Optimisation

The Merriam-Webster[6] online dictionary describes optimisation as "*an act, process, or methodology of making something (such as a design, system, or decision) as fully perfect, functional, or effective as possible*". [28] The process involves the mathematical formalisation of a quantifiable process, measurable parameter or the like, and the definition of an objective for which a solution is to be found. Through the addition of constraints one can further refine the outcome. In general there are multiple numerical optimisation methods [29, 30]. In addition, there are proven methods from the field of bionics, e.g. *Computer Aided Optimisation* (*CAO*) or *Soft Kill Option* (*SKO*) [19]. Originally derived from growth mechanisms of trees or bones, those methods are easily applied by engineers, without the need of establishing an objective function for numerical techniques.

In Design Engineering, optimisation is usually associated with the topology, i.e. the internal geometric configuration, of the part being designed. *Topology Optimisation* (*TO*) is widely used in lightweight design, where one aims to reduce or minimise the weight of a component while maintaining its shape and main functionality. Together with shape and sizing optimisation it forms the field of structural optimisation. Fig. 2.5 visualises the difference between these three methods. There are several commercially available software tools that can be used to perform structural optimisation – closely intertwined with structural simulations and the resulting stress distributions, these software vendors are usually among the typical simulation software distributors, as mentioned in Sec. 2.1.

[6] American publisher of reference books

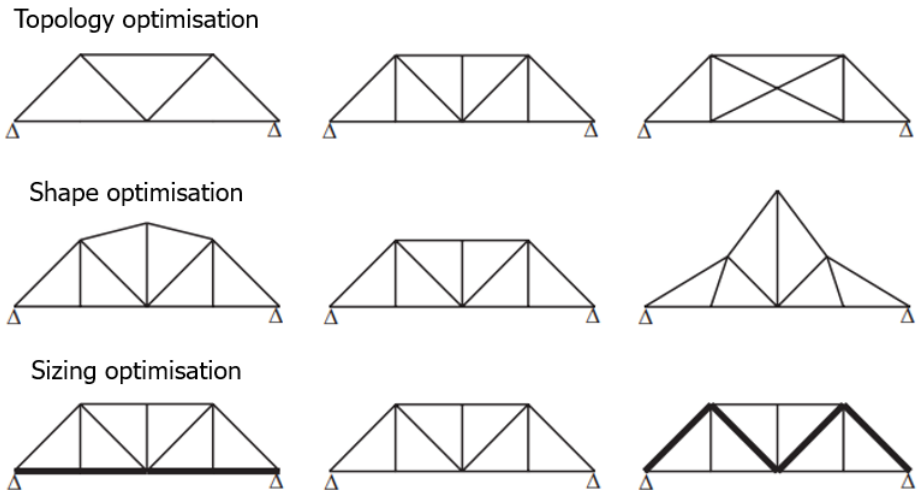

Fig. 2.5: Differentiation of the various structural optimisation types. Source: [29]

2.2.1 Optimisation Strategy

The present use-case rather demands for improved usability and functionality than optimised weight specifications, meaning the use of the mentioned *TO* software is not feasible, therefore a different approach has been designed. We aim for maximising the tangential or cable pull-out force F_x of the system, which is applied at the cable and acts in the direction of the cable axis outwards of the housing component, while limiting the allowed normal force F_N, which is used to press the clip into the cable and thus guarantees the functionality of the strain relief module. In theory, the geometry causing the highest F_x for a certain cable displacement is providing the highest functionality.

The created strategy should be easily adaptable for different use-cases involving contact mechanic problems and has the advantage of having a manageable mathematical formalism and being straightforward in application.

The steps of the method are as follows:

1. Quantification of contact forces through initial simulation
2. Mathematical formalisation of indenter geometries
3. Choosing ideal indenter geometry through numerical optimisation procedure
4. Parameter optimisation of chosen indenter geometry with *2D* and *3D* simulations

The created indenter geometry formalism was then implemented into a *Julia*[7] code to conduct the non-linear optimisation.

[7]Open source programming language highly suitable for numerical and scientific computing; https://julialang.org/

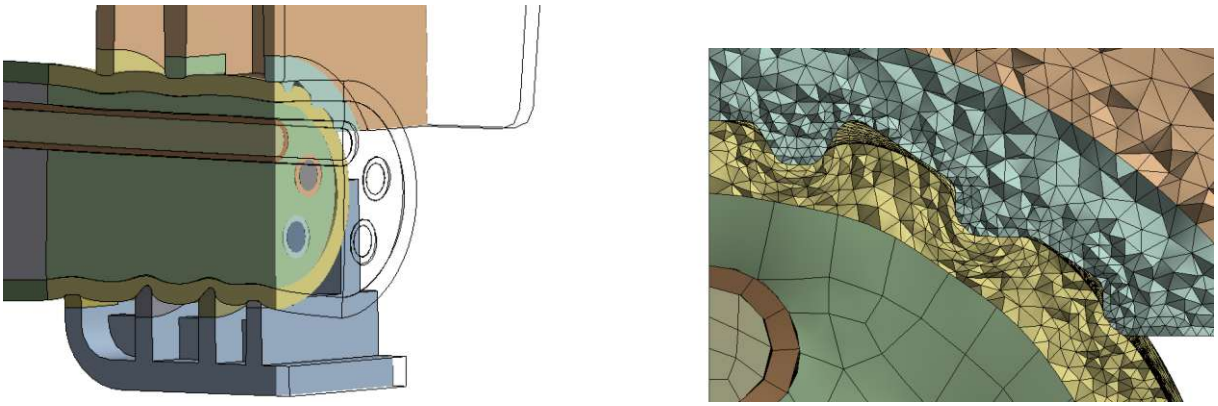

(a) Cross section of half system with displayed wire frame

(b) Detail of cross section showing teeth indentation and mesh structure

Fig. 2.6: Half system after indentation with original tension relief geometry

To apply the following optimisation algorithm several simplifying assumptions had to be made to such a degree, that the optimisation results are not equally applicable for all the differently positioned indentation bodies – let's call them teeth from here on out – of the original strain relief module. Some experience non-ideal, uneven indentation as seen in Fig. 2.6. Fig. 2.6a shows the placement of the cross section, while Fig. 2.6b shows the off-centre positioned teeth in detail. These teeth will be part of an additional parameter study performed with the *2D* and *3D* simulation capabilities of *Ansys*.

2.2.2 Method of Dimensionality Reduction

For the mathematical formulation of the indenter geometries the *Method of Dimensionality Reduction* (*MDR*) was used. As far as known to the author the method was introduced by name for the first time in 2013 in the book "*Methode der Dimensionsreduktion in Kontaktmechanik und Reibung*" [31] by Valentin Popov and Markus Hess in German language, which was followed by its English translation two years later [32] and is further detailed in [18] and [33] in English. The following description of the method closely follows this literature, and unless otherwise stated, the following formulae are taken from [33].

The method is based on the observation that certain three-dimensional contacts can be mapped to one-dimensional contacts with *Winkler foundations*, while the results remain the same. Fig. 2.7 depicts a *MDR* transformation from a three to one-dimensional contact problem, the array of individual springs or *Winkler foundation* is also visible. Through this mapping, contact problems, especially those involving axially symmetric bodies, can be simplified and solved more easily.

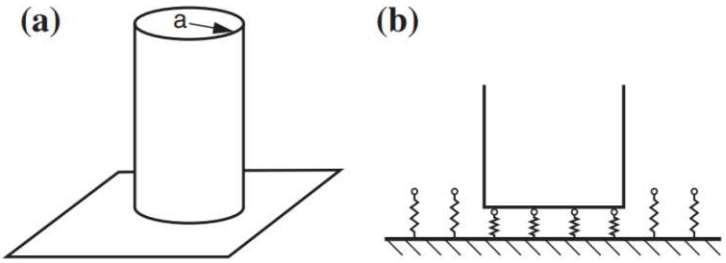

Fig. 2.7: (*a*) Three-dimensional contact of cylindrical indenter with elastic half-space; (*b*) one-dimensional system after transformation. Source: [31]

2.2.2.1 Assumptions and Limitations

The original method is applicable for axisymmetric geometries. However, subsequent papers showed that it can be applied to non-axisymmetric [34] and even arbitrary bodies [35]. The assumptions underlying the method include the following:

- Axisymmetric contact problem, i.e. ideal even indentation
- Resulting deformations or surface gradients are small (half-space approximation)
- Quasi-stationary process
- Elastic similarity of contacting bodies

Comparing the dimensions of the indenter and the indentation depth, the occurring deformations in the system are not to be regarded as small, but rather as large, which contradicts the assumption of the half-space approximation, but research showed, that it is still applicable if the thickness of the polymer surpasses the size of the contact area several times [36]. While the method allows for calculation of the stress and pressure distribution in the contact area, one should be aware, that the predicted one-dimensional contact pressure $p(x)$ and the axisymmetric value $p(r)$ of the problem pre-transformation are not directly related and surface displacements outside of the area are out of scope [27].

2.2.2.2 Formalism

First we will have a look on how to use *MDR* to describe a normal contact problem, later we'll introduce an additional load in tangential direction.

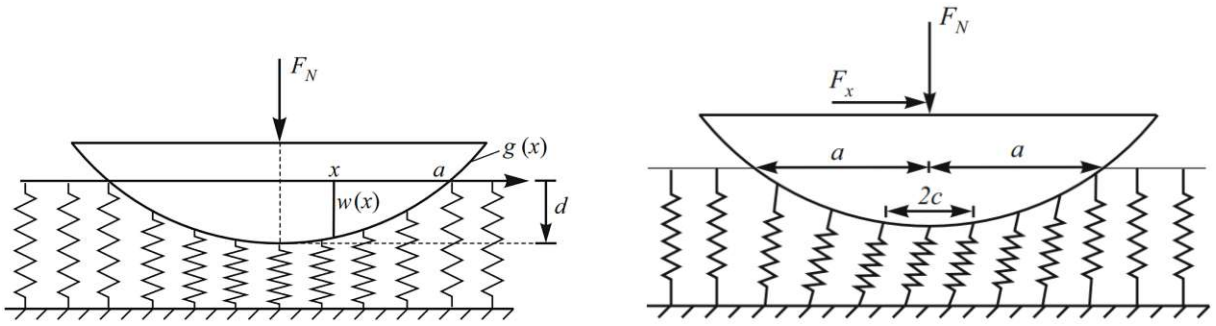

(a) Purely normal loading **(b)** Additional tangential loading with stick zone

Fig. 2.8: Depiction of *Winkler foundation* indenting bodies, as basis of *MDR*. Source: [33]

2.2.2.3 Normal Contact

To begin with, one must replace the three-dimensional elastic body to be indented with the mentioned *Winkler foundation*, a bed of linear-elastic springs, each with a normal stiffness:

$$\Delta k_z = E^* \Delta x \tag{2.4}$$

whereby E^* is the effective elasticity modulus, which results from the moduli of the contacting bodies, e.g. elastic half-space modulus E_1 and indenter modulus E_2, and their *Poisson's Ratios* ν_1 and ν_2. E^* is calculated as follows:

$$\frac{1}{E^*} = \frac{1-\nu_1^2}{E_1} + \frac{1-\nu_2^2}{E_2} \tag{2.5}$$

Δx is the distance between the spring elements and is conventionally chosen to be sufficiently small. Subsequently we transform the three-dimensional profile $\tilde{z} = f(r)$ into a one-dimensional profile $g(x)$ following the formula:

$$g(x) = |x| \int_0^{|x|} \frac{f'(r)}{\sqrt{x^2 - r^2}} \mathrm{d}r \tag{2.6}$$

The profile $g(x)$ is then indented into the array of springs with the normal force F_N, see Fig. 2.8a. The vertical displacement at position x is determined via:

$$w(x) = d - g(x). \tag{2.7}$$

The relationship between indentation depth d and contact radius a is given through the boundary condition that at the extremities of the contact zone, $x = \pm a$, the displacement must be zero:

$$w(\pm a) = 0 \Rightarrow d = g(a). \tag{2.8}$$

If we were to calculate the force of a single spring, it would result to:

$$\Delta F_N(x) = \Delta k_z w(x) = E^* w(x) \Delta x \tag{2.9}$$

and thus for $\Delta x \to 0$, we get:

$$F_N(x) = E^* \int_{-a}^{a} w(x) \mathrm{d}x = 2E^* \int_{0}^{a} (d - g(x)) \mathrm{d}x \tag{2.10}$$

for the normal force.

2.2.2.4 Tangential Loading

Now, in addition to purely normal loading, we apply a force F_x that acts in tangential direction x as seen in Fig. 2.8b. We advance analogously to the previous steps, but this time the spring elements have to counteract a force in the shearing direction, which means that their tangential stiffness amounts to:

$$\Delta k_x = G^* \Delta x \tag{2.11}$$

with the effective shear modulus

$$\frac{1}{G^*} = \frac{2 - \nu_1^2}{4G_1} + \frac{2 - \nu_2^2}{4G_2}. \tag{2.12}$$

The respective shear modulus is calculated through:

$$G_i = \frac{1}{2(1 + \nu_i)} \cdot E_i \tag{2.13}$$

and finally we get

$$\Delta F_x(x) = \Delta k_x u^{(0)} = G^* \Delta x u^{(0)} \tag{2.14}$$

whereby $u^{(0)}$ is the tangential displacement due to F_x. A specific spring sticks to the indenting body if the tangential force is lower than $\mu\Delta F_N$. We use this context to determine the radius of the stick zone c, by multiplying Eq. 2.9 with μ and equating it with Eq. 2.14:

$$G^*|u^{(0)}| = \mu E^*(d - g(c)). \tag{2.15}$$

If we set $c = 0 \rightarrow g(c) = 0$ in Eq. 2.15 we can determine the displacement when the stick zone vanishes and complete slip occurs:

$$u_c^{(0)} = \mu \frac{E^*}{G^*} d. \tag{2.16}$$

Eq. 2.16 shows that $u_c^{(0)}$ is independent of the shape of the indenter. We will use this value later on, to define the maximum permitted displacement in our system without full slip. After some further transformations we obtain the formula for the tangential force:

$$F_x = \mu[F_N(a) - F_N(c)]. \tag{2.17}$$

With these equations the "*(...) contact problem is completely defined when the shape of the indenter and one macroscopic quantity from each trio* $\{d, a, F_N\}$ *and* $\{u^{(0)}, c, F_x\}$ *are known*" [33].

2.2.2.5 Non-Axisymmetric Bodies

The method can easily be adapted to be applicable for shapes that deviate from circular cross sections, i.e. are somewhat asymmetric, by multiplying a shape-dependent constant β to the normal stiffness [37], [38]. The alternative normal contact stiffness is given by:

$$\tilde{k} = \beta 2E^* \sqrt{\frac{A}{\pi}}, \tag{2.18}$$

where A is the area of the contact. Literature shows, that $\beta \rightarrow 1$ for higher polygonal order cross sections, while it is at its maximum of 1.061 for the triangular cross section.

2.2.3 Parameter Study with *Ansys*

For teeth positioned far from the symmetry plane of the system, uneven indentation occurs. For these odd positions, we created *2D* and *3D* simulation subsystems in order to further adjust and optimise the individual parameters outside the *MDR* algorithm, which was not applicable for

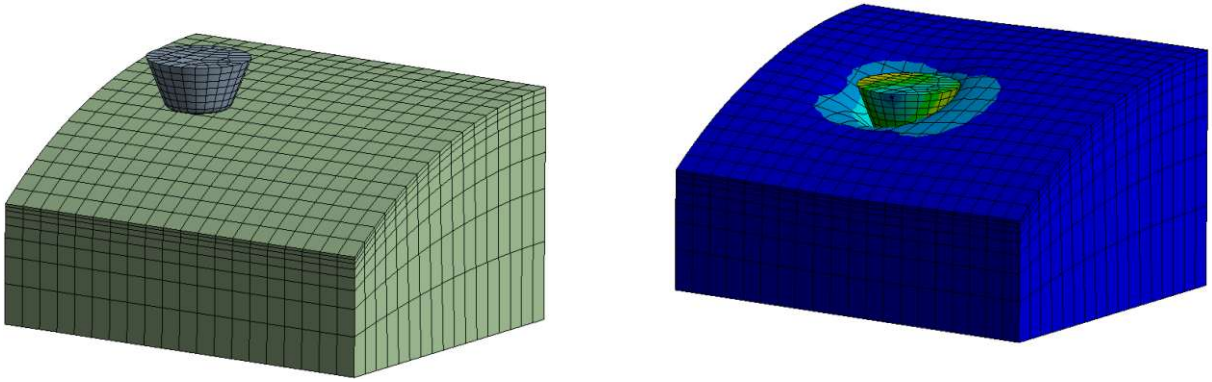

(a) Starting position of the subsystem for optimal cone angle determination

(b) Representation of the Mises stress in the system after application of a normal and a tangential load

Fig. 2.9: Visualisation of exemplary subsystem with truncated cone shaped tooth, elastic half-space and resulting deformation

these teeth. As seen in Fig. 2.9, these subsystems are kept very simple to reduce the calculation time to a minimum and to allow the investigation of different parameters in a feasible time frame. In addition we compare the new shapes with the original ones which are currently used in the system. The output parameters to be compared are:

- the ratio between the tangential force and the normal force F_x/F_N. We shall call this the *usability*, it accounts for 40 % of the total value.
- the ratio between the tangential force of the specific tooth geometry and the maximum tangential force at the tooth position under examination F_{xi}/F_{xmax}. We shall call this the *functionality* of the system, which makes up the remaining 60 % of the total value.

The *functionality* is meant to be an indicator of the likeliness of the system to withhold a certain pull-out force. The strain relief geometry is best when the applied cable displacement yields the highest retention force, if sliding occurs the retention force has probably reached its maximum and won't increase any further. However, a subsequent evaluation has shown that this is not always the case. Nonetheless, the *functionality* has to be maximised in order for the standardised tests to be successful. The *usability* links the necessary force applied by the assembler with the holding or tangential force F_x derived from it. A high ratio means less force input is needed when applying the strain relief and therefore a more pleasant interaction is offered. These two outputs are then weighted to calculate the *value* of the design point: $value = 0.6 \cdot functionality + 0.4 \cdot usability$. Of each specific tooth geometry the maximum overall occurring normal Force F_N and the maximum tangential force F_x are used for the calculation. The maximum normal Force acts after the

normal displacement has been completed and the maximum tangential force acts at the end of the tangential displacement right before full sliding occurs.

2.3 Experiments

This chapter is dedicated to the experiments which were conducted as part of this work.

2.3.1 Confocal Laser Scanning Microscopy

Since the provided *3D CAD* model was not fitted with fillets at the contact zones – sharp corners and edges lead to stress singularities – these had to be reworked. The chosen approach for this task included using confocal laser scanning microscope (*CLSM*) images [39] of the strain relief module to deduce the fillet radii at the teeth due to the manufacturing process, respectively its limitations.

2.3.2 Material Properties Deriving Experiments

In the course of the project, we conducted two major series of experiments to derive the material properties of the cable sheathing material *PVC-P*.

2.3.2.1 Neo-Hooke Model

The first experiments were done to define the *Neo-Hooke* hyperelastic material model, which is one of the only ones applicable with data from tests of a single loading mode. The reason for this was the lack of material samples for a more extensive design of experiments (*DOE*). For the experiment a ZwickiLine and a ProLine machine by ZwickRoell[8] was used. The bigger ProLine was needed due to the limited range of movement of the smaller machine and the high strains before the flexible material reached the point of failure. The specimen were manually gutted cable sheaths, which were mounted in the test rigs similar to the cables of a cable car at its drive. Fig. 2.10a shows the cross section of such a cable before the copper wires and their insulators were pulled out. Through the *DOE* we specified

- a 10 mm/s strain rate,
- and that the experiment is repeated four times to test variability.

[8] https://www.zwickroell.com/products/static-materials-testing-machines/universal-testing-machines-for-static-applications/

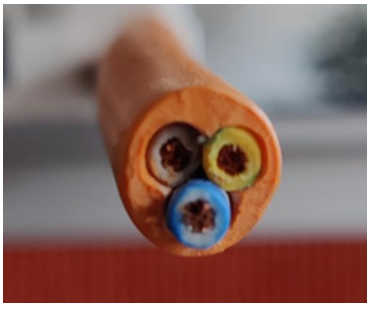

(a) Cross section of a *H05VV3x1.5* cable

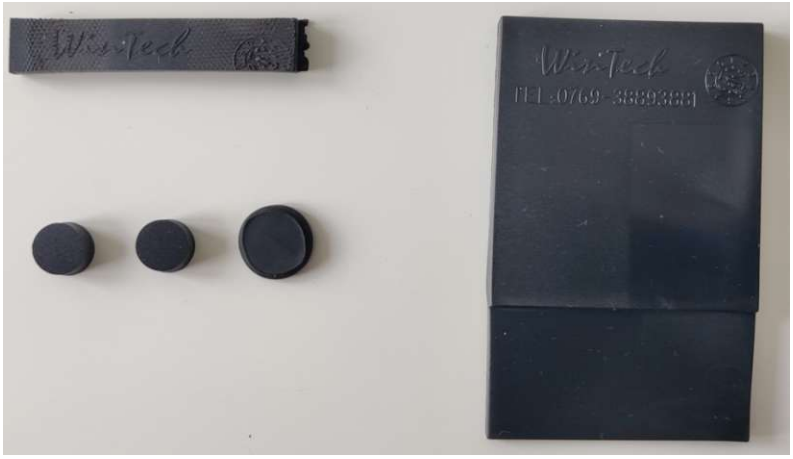

(b) Material sample with cut out specimen for tension and compression tests

Fig. 2.10: Overview of used items for the material experiments

The output is the Force in *Newton* N over displacement in *millimetres* mm. For the material model these values are transformed into engineering stress and strain [24].

2.3.2.2 Three-Network Model

Since it was possible to obtain proper material samples in the later stages of the project, the door was opened for the calibration and application of a more sophisticated material model. While the machines used have remained the same, the experimental routine for the *TN-model* is much more complicated than for the *Neo-Hooke* model and had to be adapted. To properly describe a viscoplastic material behaviour one should provide data from different loading modes and several strain rates [24]. The routine chosen for the experiment was based on the online article about "*smart mechanical testing of polymers*" [40] by Dr. Bergström. It involves the application of cyclic loading and unloading and intermediate phases of relaxation before the material is optionally brought to failure. Tension and compression were chosen as load modes for the experiment and have been carried out, as far as possible, in accordance to known standards [41], [42], [43].

The *DOE* specifies:

- tension and compression as the two chosen loading modes with test specimen as seen in Fig. 2.10b,
- strain rate of ± 0.05 $\%/s$,
- for tension:

  - 5% strain → 1 *min* relaxation phase → unloading to 0 N
  - 10% strain → 2.5 *min* relaxation phase → unloading to 0 N
  - 50% strain → 2.5 *min* relaxation phase → unloading to 0 N
  - loading until failure
- for compression:
  - −5% strain → unloading to 0 N
  - −10% strain → unloading to 0 N
  - −50% strain → unloading to 0 N
  - −70% strain
- carried out 3 times to test variability.

The output parameters remain unchanged.

2.3.3 Coefficient of Friction

We already mentioned the known laws of friction in Sec. 2.1, which are also considered in this section. In the simulation model we have several contact regions with friction, where defining a reasonable *COF* is essential for a correct description of the system. To derive the *COF* experiments were conducted by the Tribo Design department of V-Research GmbH[9] on a tribological friction and wear testing device. For the setup a *PVC-P* sample was oscillatory moved on a *100Cr6* metal plate with a mean surface roughness depth of $R_z = 1$ μm, see Fig. 2.11a. While the frequency or velocity was kept constant, the pressure was increased in specified steps. This was done since the *COF* is dependent on the applied normal force which is especially measurable for hard sliders on soft plastics [44]. The *DOE* specified the following:

- the experiment was conducted with two different material samples,
- the steps were differentiated by pressure values of the set $[0.5, 1, 2, 3, 4, 5, 7.5, 10, 12.5, 15, 20, 25]$ in N/mm^2,
- the oscillation had a frequency of 0.17 Hz with an average sliding speed of 4 mm/s,
- every step was repeated for 5 cycles.

[9] Non-university centre of excellence for applied research, URL: https://www.v-research.eu/

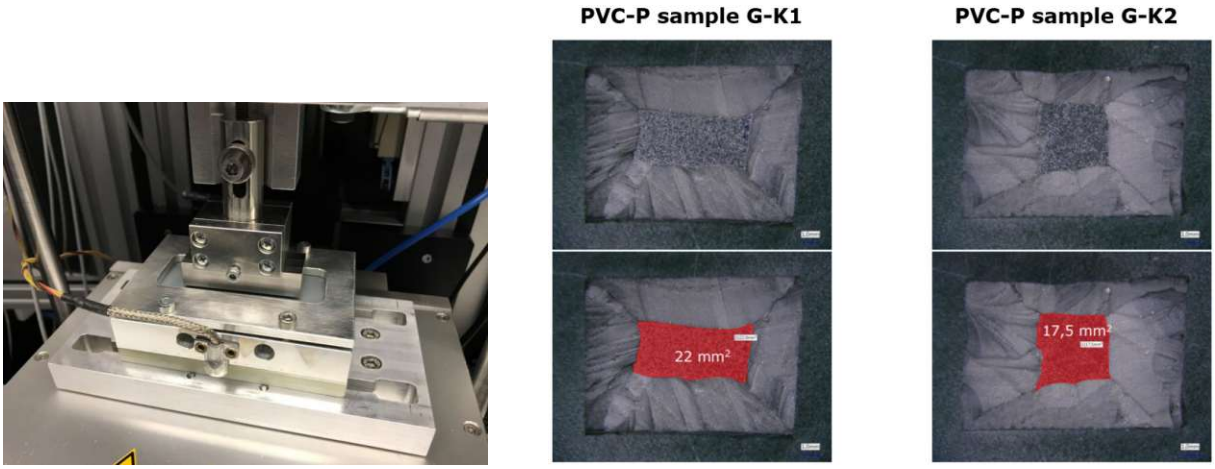

(a) Close up of the machine setup for *COF* determination

(b) *PVC-P* samples with optical determination of surface area

Fig. 2.11: Visualisation of the setup and specimen used for the experiment

The applied normal force and sliding frequency were the input parameters of the machine. To convert the applied force into pressure, the contact area of the *PVC-P* slider was determined by optical measurement, see Fig. 2.11b. As output we received the static or dynamic *COF* over the applied pressure.

2.3.4 Pull-Out Experiments

The last couple of experiments we ought to mention were performed to define a crucial part of the first load step in the simulation and validate its results. For the experiment several different cable types were fixed in the strain relief mechanism and the force to pull them out was measured. The cable properties are defined and differentiated by international standards [45], for the *FEA* their most important distinguishing feature was the amount of copper wires inside, their cross-sectional dimensions and the outer diameter of the cable. For the fixing force an educated guess of the maximum pinching force of a human thumb was made after a short review of the available literature [46]. The machine used for the controlled fixing and the pull-out experiments was a ZwickiLine by ZwickRoell. The relative position of the clips to the housing was measured regarding their latched in position after the thumb force was applied and released again, documented and later used as the final position of the clips in the simulation. Fig. 2.12 visualises this step. The relative position of the clip to the housing can be easily determined by the number of notches required until the final, latched position is reached.

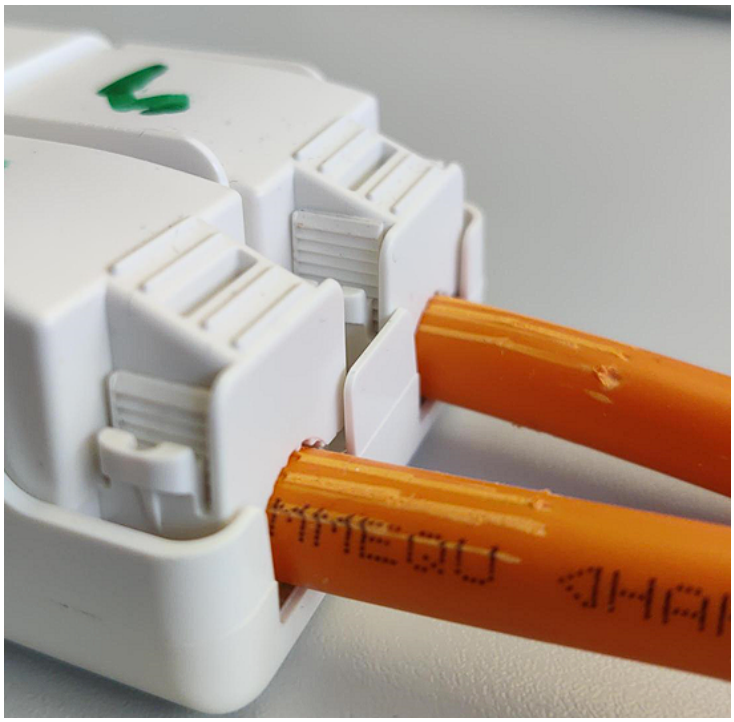

Fig. 2.12: System after a pull-out test

The results of the experiments showed that the loss of function of the strain relief mechanism, i.e. the cable is pulled out and no longer held in position, goes hand in hand with the scratching or damaging of the cable sheath surface, see Fig. 2.12. This sort of damage doesn't occur in the standard tests as the point of material failure is not reached. To describe the point of yielding or breaking different criteria are known [20, 47–49], which can be categorised as phenomenological experience-based or micromechanical models. A phenomenological model is generally not capable of predicting the true behaviour of a polymer, e.g. the Tresca or the Mises stress criterion regarding polymer shear yield behaviour [50], but it might prove a correlation between stress and material failure for some specific load conditions, while micromechanical models use the information and knowledge about the microstructure of the material but introduce additional difficulties due to the complexity of the deformation characteristics of the molecular microstructure [24]. For simplicity, however, the stress distributions of the models are compared with the Mises stress criterion, which should suffice for qualitative statements, since all models are evaluated with the same criterion and it is likely that an overall favourable stress distribution according to a given criterion will also behave similarly in the others.

Chapter 3

Results

In this chapter we'll have a look on the results of the previously elaborated and performed methods and experiments. For the following results the use-case with the cable type *H05VV-U5G1.5* was examined. We keep the basic structure from chapter 2 to a large extent, but reverse the order of the main sections and start with the experimental results, as they will be used in the optimisation process and the *FEAs* and the optimisation results are in turn used in the analyses.

3.1 Experiments

3.1.1 Confocal Laser Scanning Microscopy

Fig. 3.1 shows one of the resulting images of the experiment. It is an adapted detailed frontal view on one of the tooth rows of the clip component to measure the radii of the tooth fillets. As the figure shows, an interval of 500 μm has been divided into 5 equal parts to accommodate circles with a radius of 0.1–0.2 mm. The fillets of the teeth can be approximated by either one of those circles, depending on the flank side of the individual tooth. Since a variable fillet radius for the contact zones of the simulation models is not wanted, the lower of the two values, 0.1mm was chosen.

3.1.2 Material Properties Deriving Experiments

For both material models similar experiments were conducted. Since the *Neo-Hooke* model was superseded by the *TNM* and the experiments for the new model were more sophisticated, we shall have a look on these results. Fig. 3.2 shows the stress-strain curves of the three samples tested according to the *DOE* in section 2.3. It can be seen that the samples initially showed similar behaviour and the results diverged noticeably during the last loading cycle. For strains above

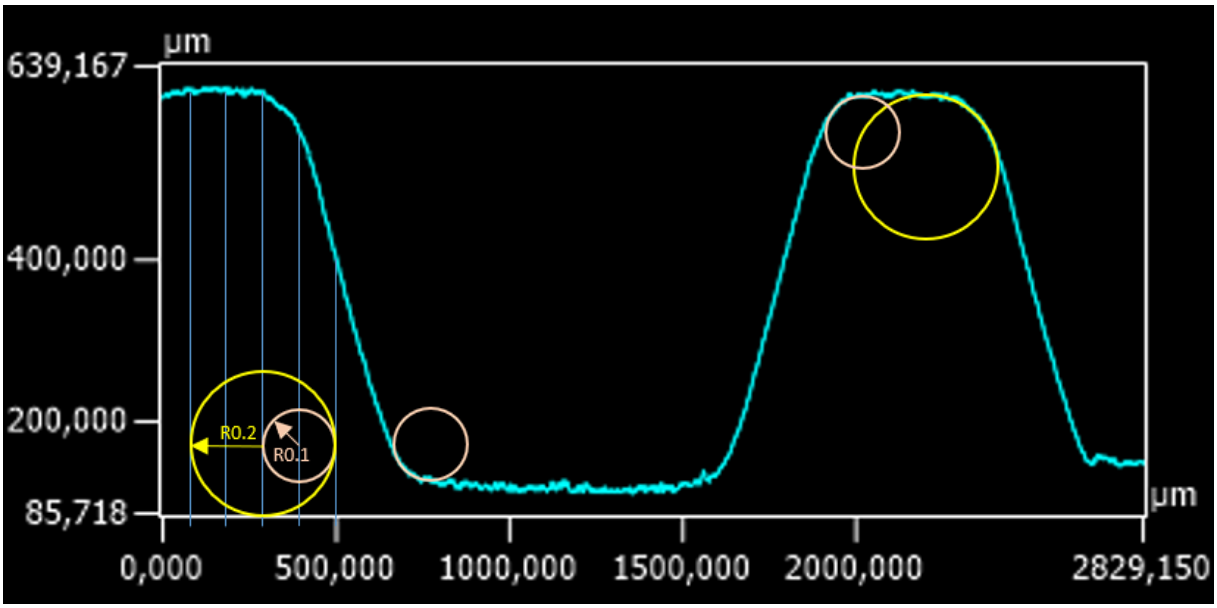

Fig. 3.1: *CLSM* result with added graphical evaluation tools

300% of the original specimen length, there is a significant deviation which need not concern us as such strains do not occur in the simulation – they are limited to around 200%. The stress drops starting at around 350% elongation and above are due to the specimens slipping out of the clamping jaws of the machine. Further tensile experiments where only the cable sheath was loaded showed that the *ultimate tensile strength* (*UTS*) of the material is about 10.64 MPa at around 650 % elongation. To calculate the initial *Young's Modulus* of the material we take an interval of the first linear ascend of the stress-strain curve and compare the resulting stress with the corresponding strain, $E = \frac{\sigma}{\epsilon} = 13.61$ N/mm^2. The compression experiments show similar results in terms of data variability, see Fig. 3.3. It can be seen that the stress responses show a small deviation at small strains, while it increases with growing compression.

3.1.3 Coefficient of Friction

Fig. 3.4 shows the mean value results of the two friction experiments. We can see that for increasing pressure the static *COF* strives towards a limit value of around 0.47, or respectively 0.5 for the dynamic *COF*, and the variance between the different measurement cycles decreases. For the simulation model we distinguish between three different pressure zones, see Tab. 3.1. This is subsequently used to define the frictional contacts of the system.

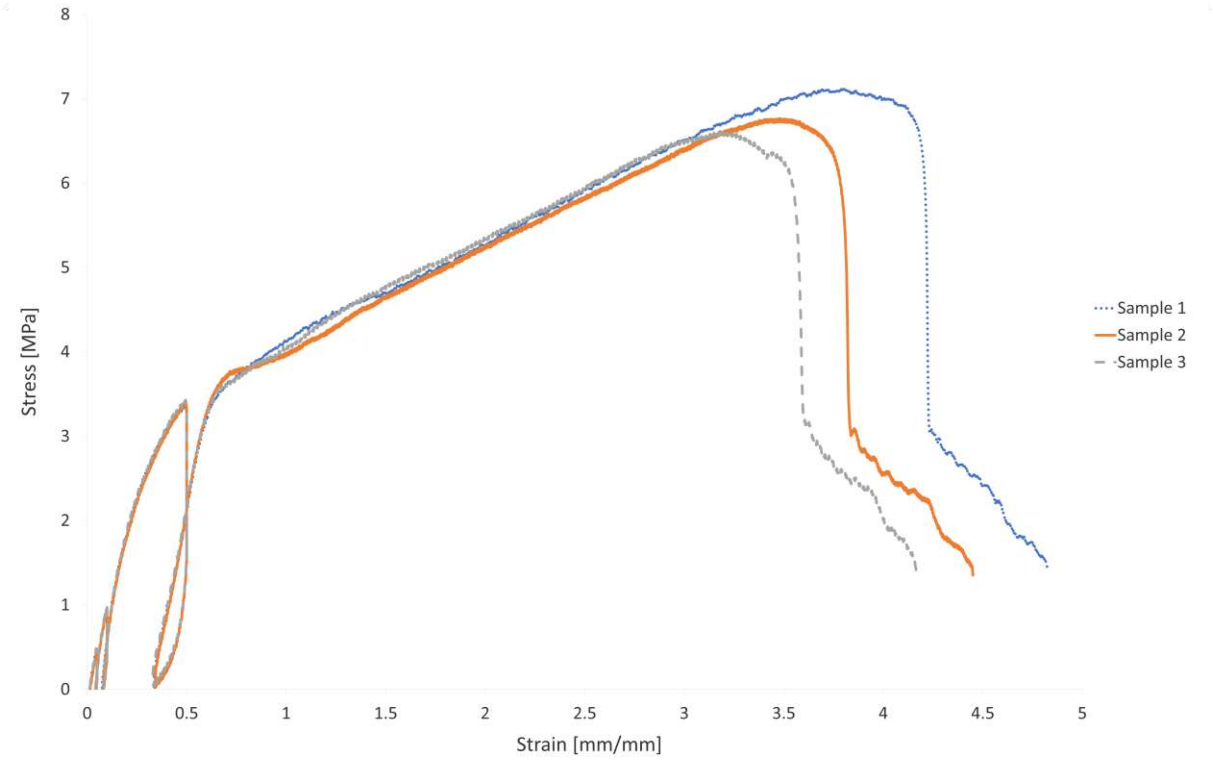

Fig. 3.2: Stress-strain results of the tensile test for the *TNM*

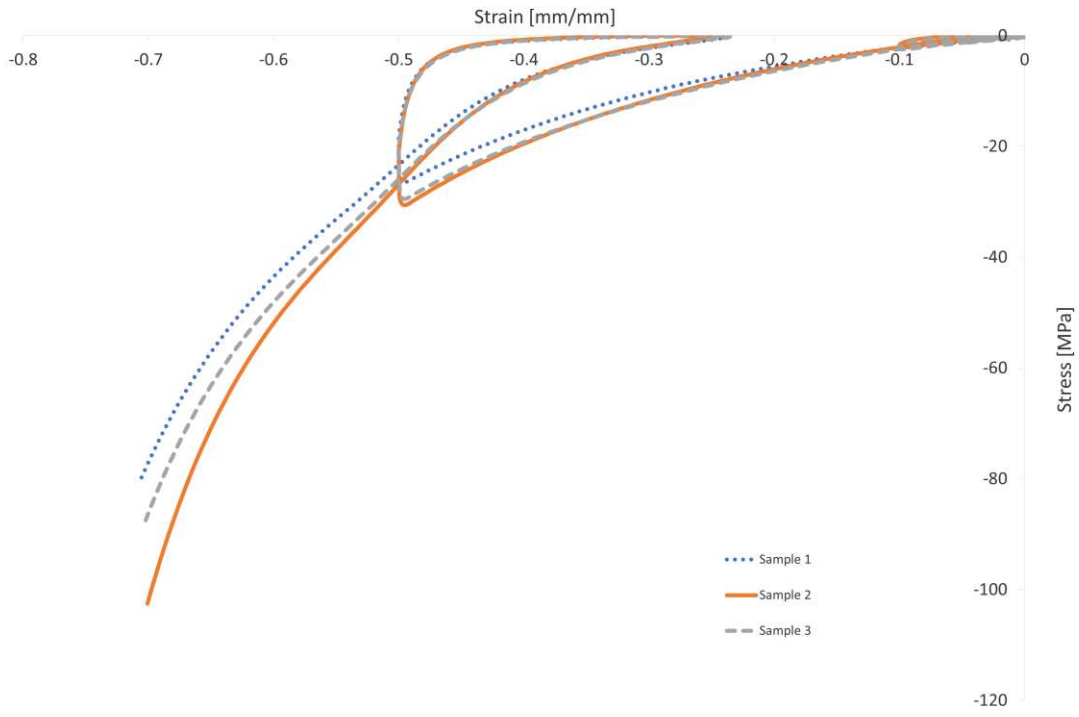

Fig. 3.3: Resulting curves of the compression test for the *TNM*

Tab. 3.1: Average values for the static *COF* for specified pressure ranges

ID	Pressure range [N/mm^2]	Static *COF*
1	0.5–5	0.75
2	5–20	0.52
3	20 and above	0.48

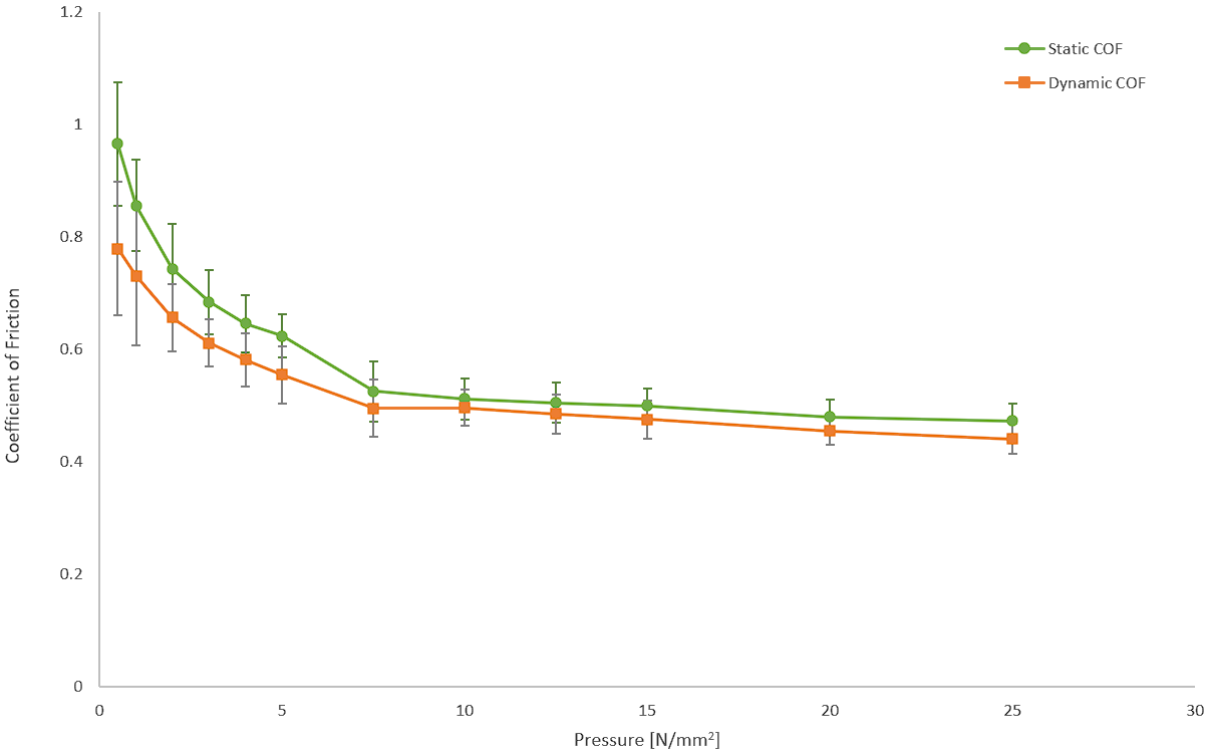

Fig. 3.4: Averaged result of the two friction experiment samples

3.1.4 Pull-Out Experiments

The clips were pressed into the cable and onto the mounting of the housing with a force of 120 N. Tab. 3.2 shows the pull-out force of the different types of cables and the clip position, quantified with the number of notches that were passed until the clip reached its final snap-in position. These results can later be used to validate the simulation results. Also the later required indentation depth d can be derived through the notch position.

Tab. 3.2: Results of the pull-out experiments

Cable type	Notch position	Pull-out force [N]
H05VV-U5G1.5	5	131
H05VV5x2.5U	3	180
H05VV3x1.5	6	147.8
IEC 53 (RVV) 2x0.75	10	47.2
IEC 53 RVVB 2x1.0	10	98

Tab. 3.3: Material specific input parameters of the optimisation procedure. Index "1" corresponds to the *PVC*, index "2" to the *PC*

ID	ν_i	E_i [MPa]	G_i [MPa]	$\sigma_{\epsilon=5\%}$ [MPa]
1	0.425	13.61	4.78	
2	0.37	2400	875.9	63

Tab. 3.4: Calculated input parameters of the system

E^* [MPa]	G^* [MPa]	F_N [N]	$u_c^{(0)}$ [mm]	$u^{(0)}$ [mm]	μ	d [mm]	A_{min} [mm^2]
16.51	12.06	20	0.684	0.61	0.52	1.9202	0.32

3.2 Optimisation

3.2.1 Calculation of Required Parameters

Tables 3.3 and 3.4 show the resulting parameters of the system required as input for the optimisation procedure. The respective *Poisson's Ratios* were estimated in accordance to literature [51] or taken from respective data sheets, while the *E-moduli* were either given or calculated through the experiment outputs. The effective elasticity modulus is calculated according to Eq. 2.5, the effective shear modulus according to Eq. 2.12, the maximum permitted displacement before full slip occurs according to Eq. 2.16. For the calculation of the normal and tangential forces a tangential displacement $u^{(0)} < u_c^{(0)}$ is chosen and defined in Tab. 3.4. In addition, we have derived a minimum indenter tip surface area $A_{min} = \frac{F}{\sigma}$ to remain below a 5 % strain threshold and its corresponding stress – after evaluation of the simulation results the maximum occurring normal force at a contact interface is chosen to be 20 N.

3.2.2 Optimisation Algorithm

Several profile functions have been implemented into a *Julia* code routine to determine the best shape for the indenter geometry in a comparison. Fig. 3.5 provides an overview of the

different examined profiles. We shall have an exemplary look on the *MDR* solution of the normal contact problem of a cone shaped profile, see Fig. 3.5c, and compare it to the three-dimensional result to see if they are indeed identical as claimed by inventors of the method:

The shape of a cone is defined through the equation $f(r) = r \cdot \tan\theta$. Using Eq. 2.6 we obtain $g(x) = \frac{\pi}{2} \tan\theta \cdot |x|$ after applying the *MDR* transformation. If we press the cone into the winkler foundation we can describe the displacement with $u_z(x) = d - \frac{\pi}{2} \tan\theta \cdot |x|$, according to Eq. 2.7, and via $u_z(a) = 0$ we calculate the contact radius $a = \frac{2}{\pi} \frac{d}{\tan\theta}$. Using Eq. 2.10 we obtain $F_N = \frac{2E^*}{\pi} \frac{d^2}{\tan\theta}$, which is identical to the three-dimensional solution [52].

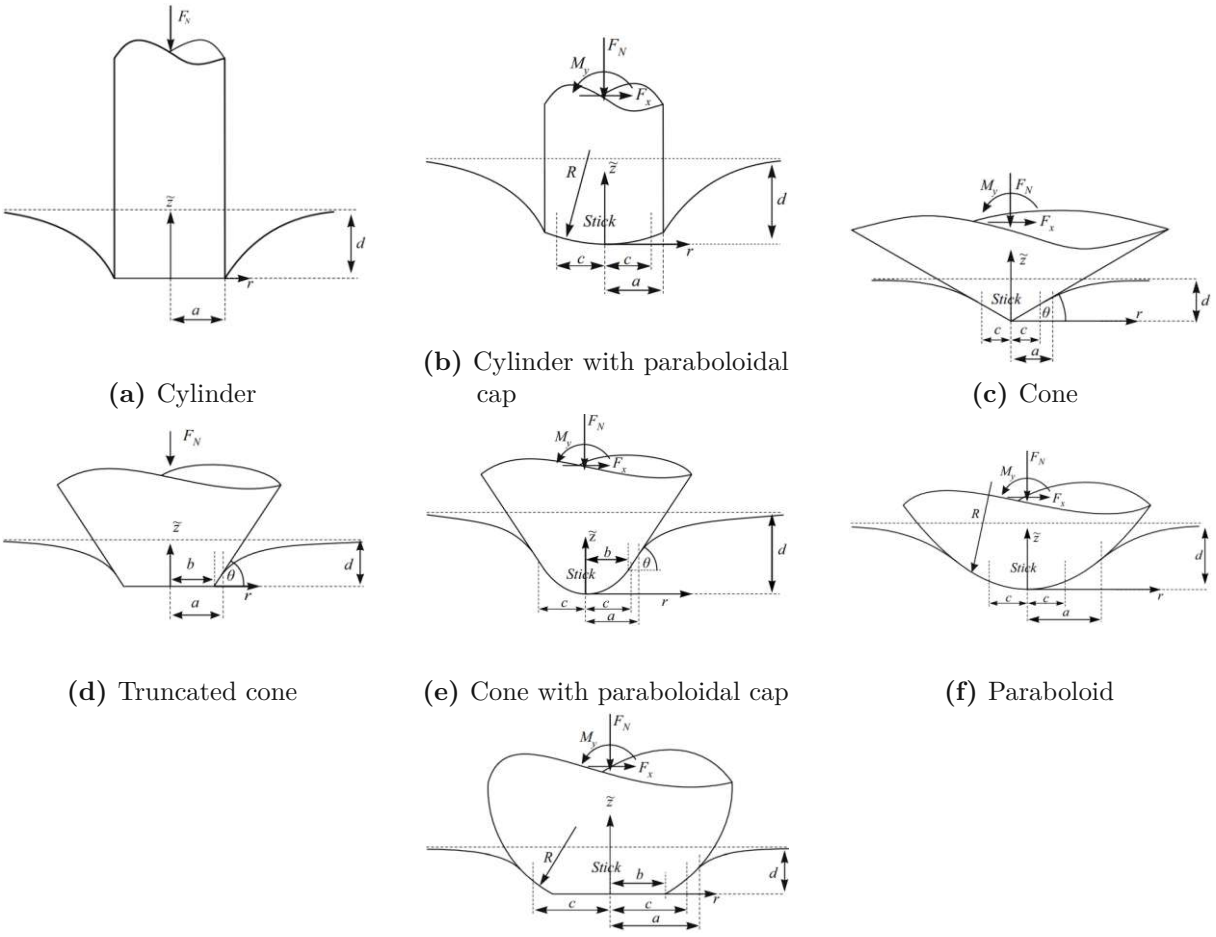

(a) Cylinder

(b) Cylinder with paraboloidal cap

(c) Cone

(d) Truncated cone

(e) Cone with paraboloidal cap

(f) Paraboloid

(g) Truncated paraboloid

Fig. 3.5: Overview of the different profile shapes. Source: [33]

Tab. 3.5 shows the analytical resulting normal force F_N of all the profiles examined. With Eq. 2.15 and 2.8 we can calculate our stick zone radius c and use Eq. 2.17 to determine the

Tab. 3.5: Functions $F_N(x)$ and $d(x)$ of the different profiles. Source: [33]

Profile	$F_N(x)$	$d(x)$
Cylinder	$2E^* d\ x$	–
Cylinder with paraboloidal cap	$2E^*(d\ x - \frac{x^3}{3R})$	–
Cone	$\frac{\pi x^2}{2} E^* \tan\theta$	$\frac{\pi}{2}\ x\ \tan\theta$
Truncated Cone	$E^* \tan\theta\ x^2[\arccos(\frac{b}{x}) + \frac{b}{x}\sqrt{1-\frac{b^2}{x^2}}]$	$a\ \tan\theta\ \arccos(\frac{b}{x})$
Cone with paraboloidal cap	$\frac{E^* x^2\ \tan\theta}{b}[b\ \arccos(\frac{b}{x})$ $+\frac{4}{3}(x - \sqrt{x^2-b^2} + \frac{b^2\sqrt{x^2-b^2}}{3a^2})$	$\frac{x}{b}\ \tan\theta[x - \sqrt{x^2-b^2}$ $+b\ \arccos(\frac{b}{x})]$
Paraboloid	$\frac{4E^* x^3}{3R}$	$\frac{x^2}{R}$
Truncated Paraboloid	$\frac{2E^*}{3R}(2x^2+b^2)\sqrt{x^2-b^2}$	$\frac{x}{R}\sqrt{x^2-b^2}$

Tab. 3.6: Resulting tangential force F_x of the different profiles

Profile	F_x [N]
Cylinder	9.28
Cylinder with paraboloidal cap	10.03
Cone	10.28
Truncated Cone	11.75
Cone with paraboloidal cap	10.4
Paraboloid	10.03
Truncated Paraboloid	10.37

tangential holding force F_x. For the cylinder a function for d is not especially given, since the contact interface is a straight horizontal line and therefore the indentation depth within the contact radius is equal to d and not a function of x, and for the cylinder with a paraboloid cap it is a superposition of this very fact and the paraboloidal function for d.

For some equations auxiliary variables had to be introduced in order to prevent complex results, divisions by 0, etc. during the optimisation procedure and add additional robustness to the code. The indentation depth d is halved for a specific tooth, since it is equally divided between the two cable contacting components, the clip and the housing, respectively the indentation bodies on the specific component. The codes of the other profiles can be found in the appendix of this work.

```julia
### Importing necessary packages for optimisation##
using SpecialFunctions
using JuMP
import Ipopt

### Definition of input variables ###
E = 16.51       #MPa
d = 1.9202/2    #mm; indentation depth per side
tau_0 = 29.42   #MPa
eps = 1e-6      # auxilliary variable
mu = 0.52       # COF
G = 12.06       #MPa
u0=0.61         #mm

### Definition of profile specific functions ###
function FN_Cone(d,E,G,a)
    c = a-2*G*u0/(pi*mu*E*(2*d/(pi*a)))
    FN = (pi*E*(2*d/(pi*a))*(a)^2)/2
    Fx = mu*FN*(1-c^2/a^2)
    Fx,FN,a,c
end

### Definition of objective and constraints ###
obj(a)= FN_Cone(d,E,G,a)[1]
FN(a)= FN_Cone(d,E,G,a)[2]

Cone = Model(Ipopt.Optimizer)
register(Cone, :obj, 1, obj; autodiff = true)
register(Cone, :FN, 1, FN; autodiff = true)
@variable(Cone, eps <= a <= 6)
@NLobjective(Cone, Max, obj(a))
@NLconstraint(Cone, FN(a)<=20)
optimize!(Cone)
@show termination_status(Cone)
@show primal_status(Cone)
@show dual_status(Cone)
@show objective_value(Cone)

### Output definition of optimised parameters ###
a_opt = value(a)
c_opt = a_opt-2*G*u0/(pi*mu*E*(2*d/(pi*a_opt)))
FN_opt= FN(a_opt)
Fx_opt = obj(a_opt)
theta_opt = atan(2*d/(pi*a_opt))*180/pi

C = Array{Any}(undef,1,3)
C[1,:] = [:Cone Fx_opt FN_opt]
```

Fig. 3.6: Julia code lines for the cone profile

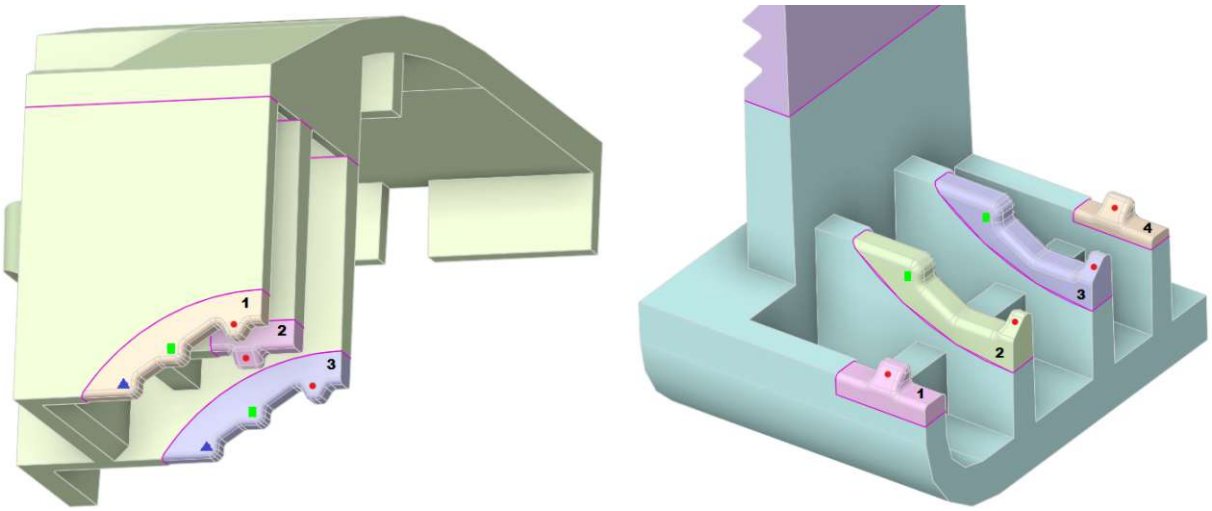

(a) View of the clamp teeth **(b)** View of the teeth on the housing

Fig. 3.7: Close-ups of the original indentation bodies on the simplified and locally isolated models of the clamp and the underside of the component's housing. Distinguishing features of the different tooth positions are: upper (U) or lower (L) , respectively clamp or housing, row number (1–4), distance from plane of symmetry (red dot [R] - green rectangle [G] - blue triangle [B])

Tab. 3.6 shows the resulting, profile specific tangential forces of the optimisation procedure. We can see, that for the input parameters, as defined in Tab. 3.3 and Tab. 3.4, the truncated cone displays the highest tangential force. Therefore, in our case, the optimal indenter shape is that of a truncated cone and will be examined in more detail in the following section. The results of the cylinder with paraboloidal cap and paraboloid are identical. It is probable, that this is due to the contact being dominantly present at the paraboloidal part of the geometry since adding the geometrical constraints of the cylinder to the paraboloid algorithm didn't lead to any restrictions. Ultimately, this will not be investigated further, as neither the result of the paraboloid nor the cylinder is as promising as that of the cone or the truncated cone and therefore no influence on the outcome of the optimisation procedure is to be expected. Fig. 3.6 shows an example of the Julia code lines to calculate the optimal parameters of the cone profile. Since we defined in the beginning, that the overall geometry of the system should be kept unchanged and only the indenting sub-geometries, i.e. the teeth, should be adapted, we use the determined optimal indenter shape of the truncated cone to perform a thorough parameter study using the *FEA* capabilities of *Ansys* while respecting the geometric constraint.

3.2.3 *Ansys* Parameter Optimisation

Besides the additional *2D* and *3D FEA* based optimisation of the geometric parameters of the truncated cone shaped indenter, we simultaneously reviewed specific non circular cross sections with possible tangential force increasing properties as mentioned in [37] and [38] – in this case triangular or square cross sections, resulting in frustum or truncated pyramid-shaped teeth – and compared them to the truncated cone and the original teeth. For the *FEAs* we used the following parameters as input for the indenting body:

- Normal displacement = 0.5mm
- Tangential displacement = 0.5mm

The original position specific orientation of the tooth to the cable surface and the minimum cross-sectional area A_{min} from Tab. 3.4 were reused.

While Fig. 3.7 visualises and labels the different tooth positions on the clamp and the housing bottom, Fig. 3.8 shows the different tooth geometries investigated and optimised. The shapes were evaluated according to Sec. 2.2.3 and in Tab. 3.7 the results are listed. All of the following discussed shapes are truncated. It can be seen that the orientation of the triangular pyramid, Fig. 3.8b and Fig. 3.8c, is affecting the value of the overall shape. Having the pyramid pointing in the direction of the tangential movement, i.e. from the inside of the component to the outside, increases the value by almost 10%. Additionally, these triangular pyramids are the only shapes that exhibit the anomaly of having a *usability* $F_x/F_N > 1$, which is of no further interest to us since these particular shapes were originally modelled not in compliance with the geometric constraints, but to determine the optimal orientation. Following on from this, the pyramid was adapted to the geometric constraints, see Fig. 3.8d, which lead to the overall best valued tooth shape, which is in line with the research mentioned in Sec. 2.2.2.5. Furthermore, the original tooth and square pyramid, Fig. 3.8a and Fig. 3.8e, are rated much worse compared to the triangular pyramid while the cone shaped bodies deviate less than 10% from the maximum value. While the alteration of the cone angle α only slightly influences the overall value of the isolated cone shape, it is suspected that wider bases and the resulting dwindling voids between the teeth due to the higher angles result in a less favourable contact between the *PVC* and the teeth and reduce the acting frictional forces, therefore the lower cone angle, i.e. $\alpha = 50°$, is chosen for tooth positions marked with a red dot, see Fig. 3.7. It should be mentioned that due to the manufacturing process of the components by injection moulding and the constraints

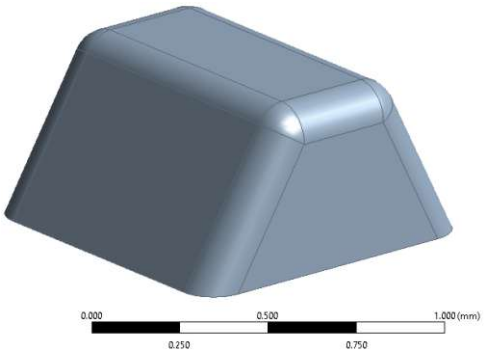

(a) Original tooth shape with size scale

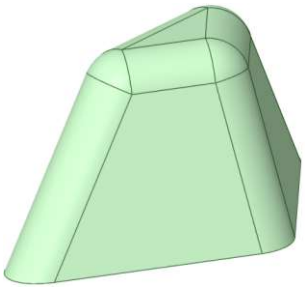

(b) Truncated triangular pyramid

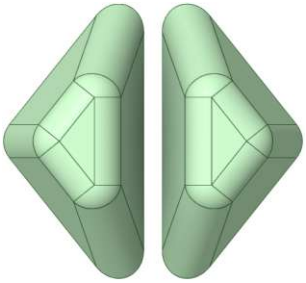

(c) Both possible triangular pyramid orientations were investigated

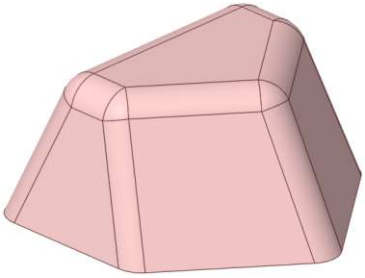

(d) Truncated triangular pyramid adapted to geometric constraints

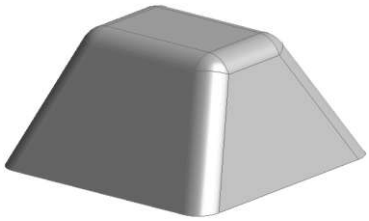

(e) Truncated square pyramid

(f) Truncated cone with $\alpha = 50°$

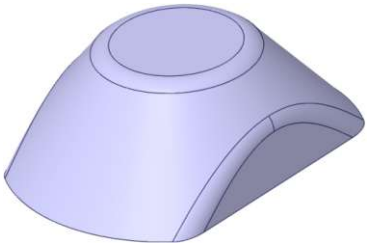

(g) Truncated cone with $\alpha = 80°$

Fig. 3.8: Overview of the different isolated tooth shapes

involved, the angle of the cones for the positions not marked with a red dot have to be adapted to allow the part to be pulled out from the mould effortlessly. For the cones at the green and blue, respectively rectangle and triangle, positions another set of *FEAs* was conducted, as the teeth are aligned differently at these positions. Possible cone angles have been compared and due to the results, see Tab. 3.8, the cone angle is chosen to be $\alpha = 70°$. For the triangular pyramid shaped teeth the adjustment was carried out analogously. The bodies with the optimised teeth are shown in Fig. 3.9.

For the final *FEAs* full models with truncated triangular pyramid shaped and truncated cone shaped teeth were designed and compared to the original model.

Shape	F_{xmax} [N]	F_{Nmax} [N]	F_x/F_N	$F_{xi}/F_{xmaxglobal}$	Value
Original	4.819	6.432	0.749	0.859	0.815
Triangular pyramid inside	3.300	3.236	1.020	0.588	0.761
Triangular pyramid outside	3.606	3.286	1.097	0.643	0.825
Square pyramid	4.295	5.218	0.823	0.766	0.789
Cone $\alpha = 50°$	5.443	7.056	0.771	0.970	0.891
Cone $\alpha = 80°$	5.402	6.780	0.797	0.963	0.896
Adapted triangular pyramid	5.611	6.197	0.905	1.000	0.962

Tab. 3.7: Results of the *3D FEA* tooth shape comparison with assumed ideal indentation

Tab. 3.8: Results of the *3D FEA* cone angle comparison for the off-centre positioned teeth

Angle [°]	F_{xmax} [N]	F_{Nmax} [N]	F_x/F_N	$F_{xi}/F_{xmaxglobal}$	Value
70	9.041	15.288	0.591	1.000	0.837
80	7.779	13.431	0.579	0.860	0.748
90	7.151	11.953	0.598	0.791	0.714

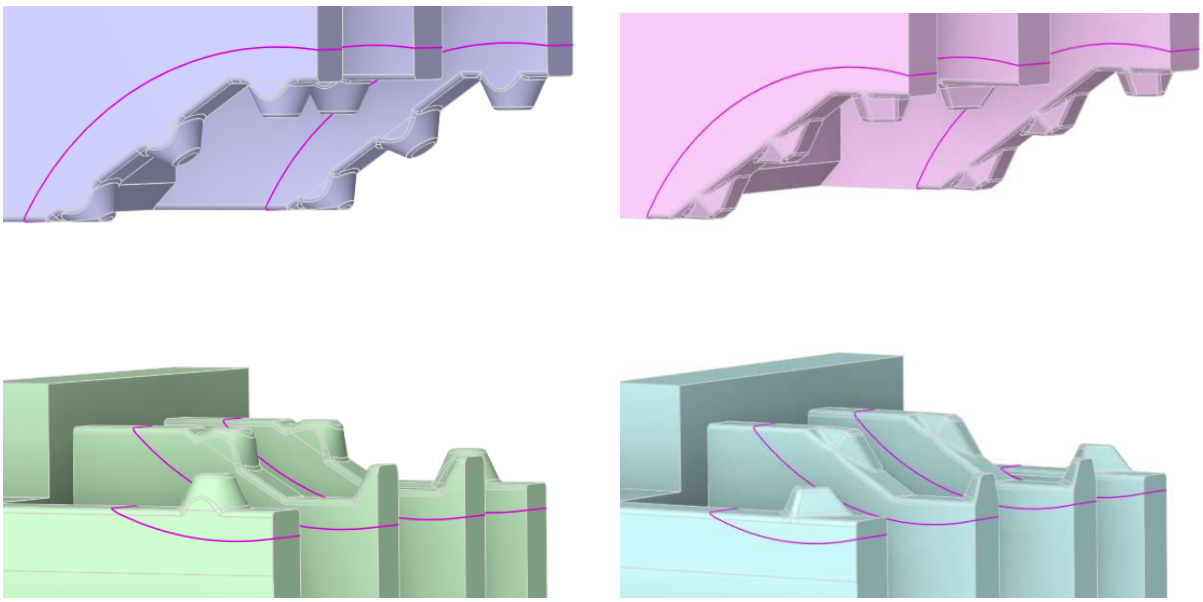

(a) Truncated cone shaped teeth **(b)** Truncated triangular pyramid shaped teeth

Fig. 3.9: Side-by-side representation of the two models with optimised indentation bodies

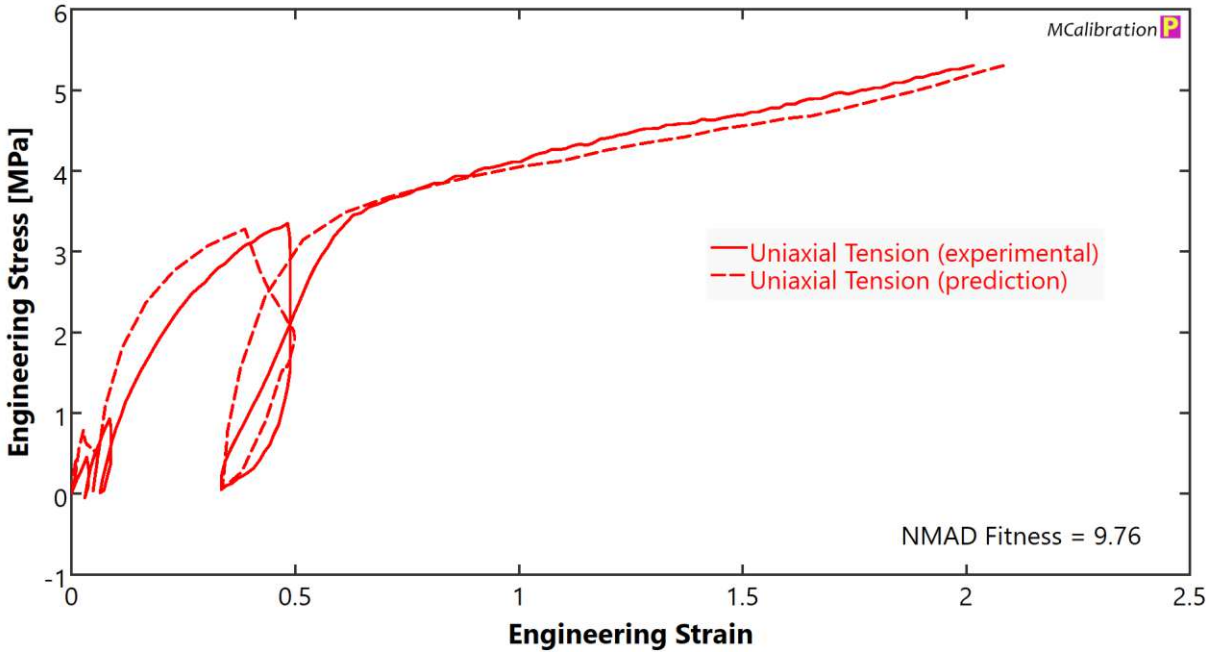

Fig. 3.10: Comparison of experimental and predicted behaviour for uniaxial tension in *MCalibration*

3.3 Finite Element Analysis

This section includes the resulting behaviour of the chosen material model, an overview of the different approaches taken to lead the model to convergence and a comparison between the models with the different strain relief geometries.

3.3.1 Material Model

To evaluate the material model we compare the experimental data with the predicted behaviour resulting through the calculated material model properties in our calibration tool *MCalibration*, using its internal solver, and reproduce the originally performed material experiments virtually by simulation and plot the results with *Excel*. Fig. 3.10 and 3.11 show the comparison between the experimental and predicted material behaviour during tensile and compressive loading as calculated and plotted in *MCalibration*. The normalized median absolute deviation (*NMAD*) fitness of the overall material model is calculated to be less than 10 % and the plots confirm the very good fit over the whole strain range.

Exporting the material model to *Ansys Workbench* for simulative validation shows a significantly different behaviour for positive strains, see Fig. 3.12. A strain of 50% results in a deviation of the stress value of over 200%, with the trend of stress discrepancy continuing and reaching

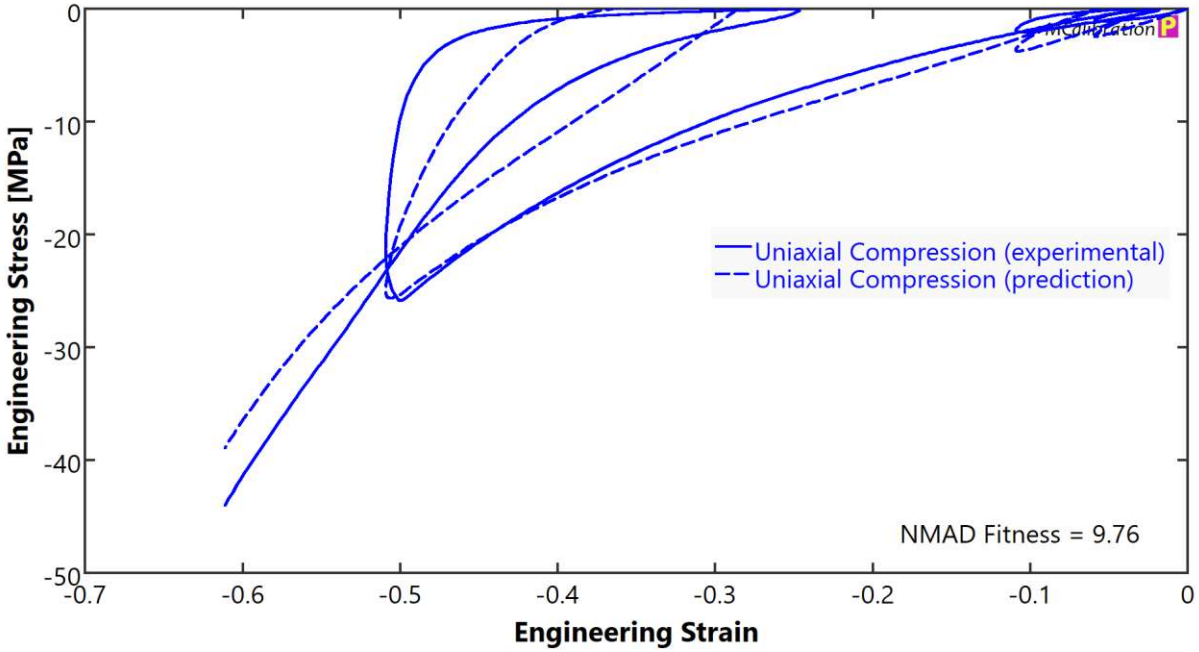

Fig. 3.11: Comparison of experimental and predicted behaviour for uniaxial compression in *MCalibration*

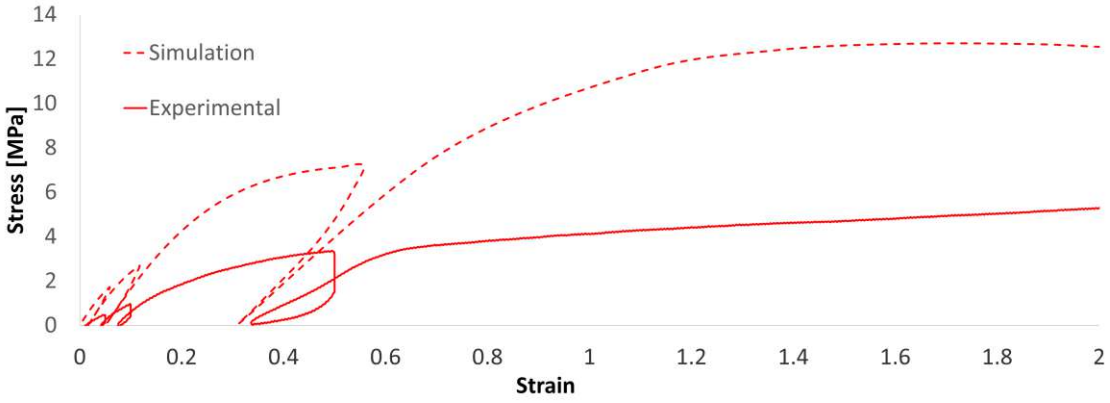

Fig. 3.12: Comparison of experimental and simulation results for uniaxial tension

almost 300% at strains above 120%. For negative strains there is a better conformity, with stress deviation never exceeding 28% under compressive loads, see Fig. 3.13.

Although the model was supposedly predicting the material behaviour with only a small error, the actual deviation lead to an adaptation of the parameters. Since the simulated behaviour overestimated the stress values over the entire strain range, the initial material parameters were reduced by half, as it offered the best compromise in keeping the errors in compression and tension relatively small between and a manual adaptation of the 16 material parameters did not seem feasible. The results are as expected, while the prediction for tensile loads is improving

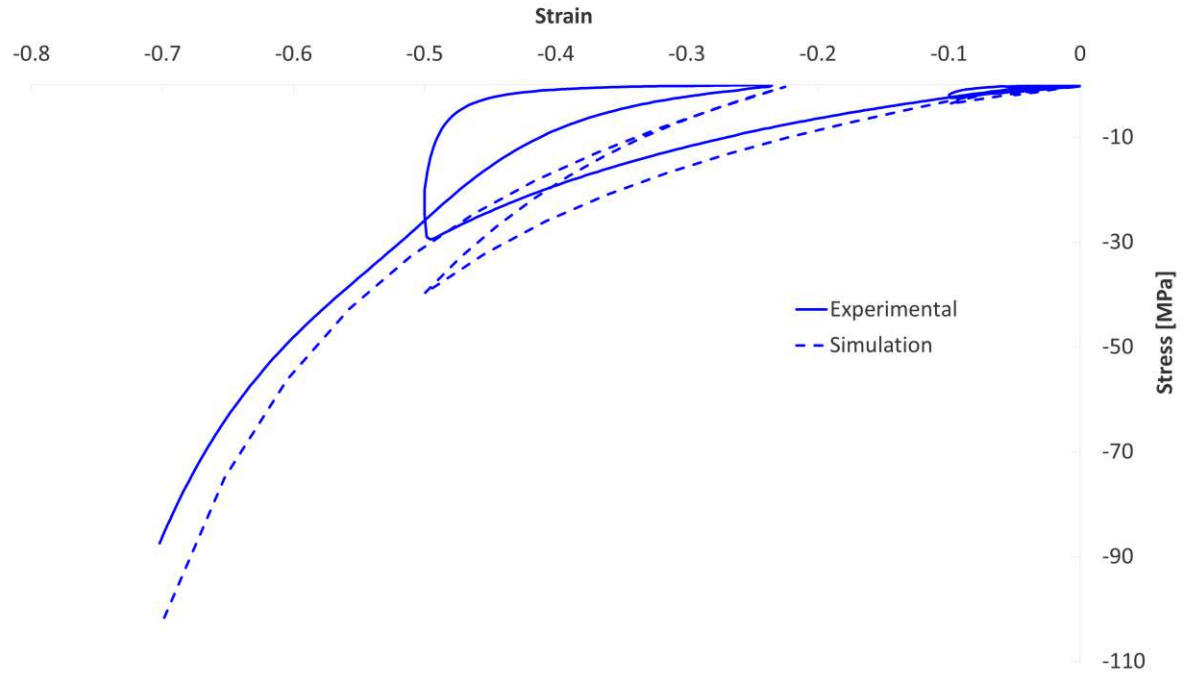

Fig. 3.13: Comparison of experimental and simulation results for uniaxial compression

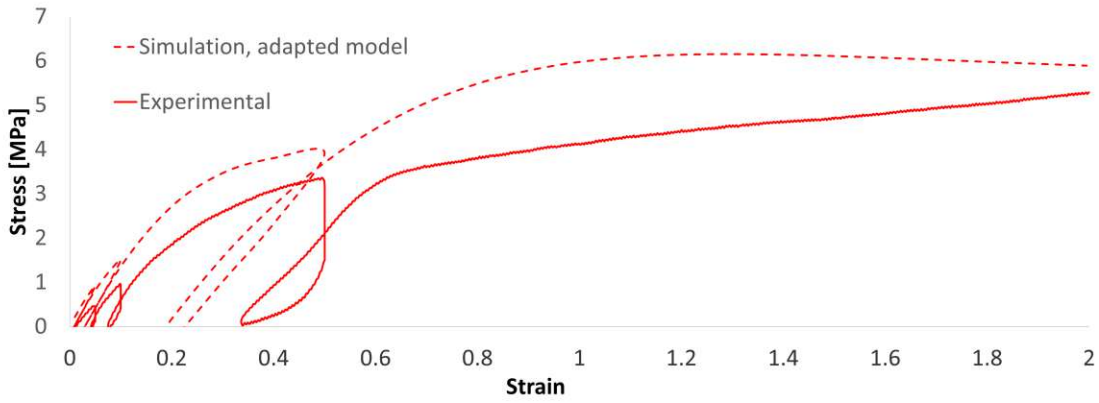

Fig. 3.14: Comparison of experimental and simulation results for uniaxial tension with adapted material model

massively with a maximum deviation of about 50% at 100% strain, see Fig. 3.14, the behaviour under compressive loads gets underestimated for around 38% at most, see Fig. 3.15. Although not perfect, the adjustment results in a better overall fit and reduces the stresses on the other components of the system due to the otherwise excessively rigid material model of the cable sheath.

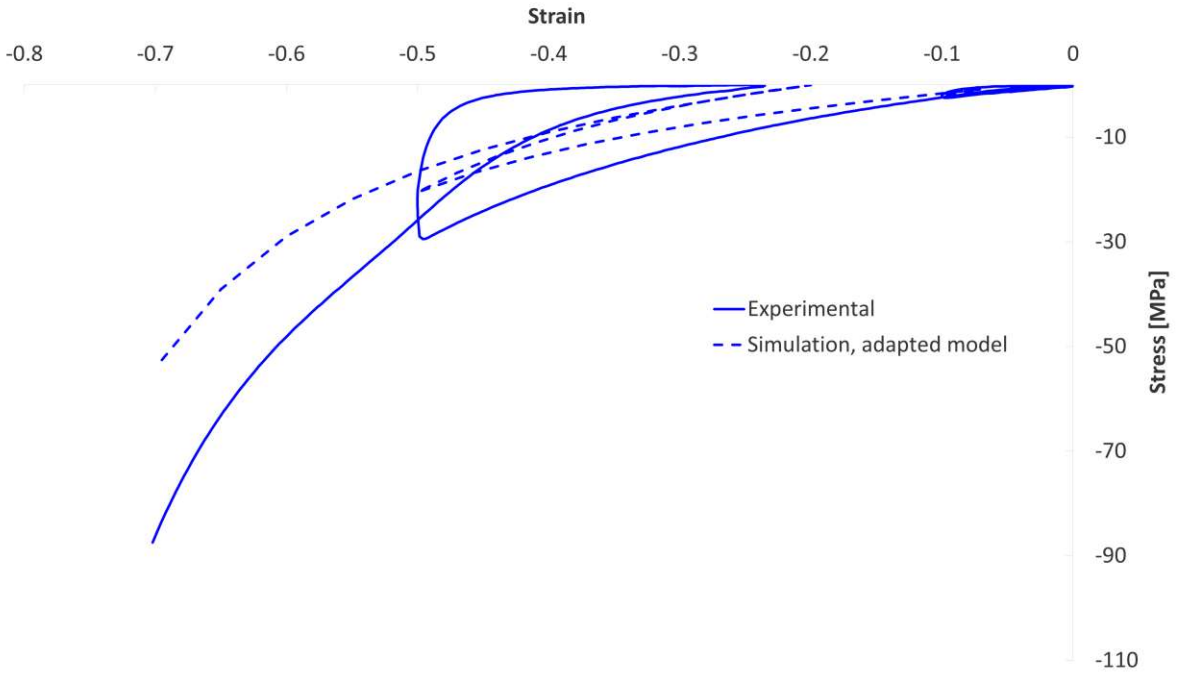

Fig. 3.15: Comparison of experimental and simulation results for uniaxial compression with adapted material model

3.3.2 Simulation

During the project the simulation model and the chosen approach for convergence and obtaining meaningful results were subject to constant change. We shall take a brief look at this evolution and the associated findings, before we compare the results in terms of *functionality*, *usability* and actual prevention of sliding of the original model with its potential successors – subsequently we shall call them cone and pyramid model.

3.3.2.1 Approach History

The very first models and approaches are not mentioned due to their low information value, as the author first had to become autodidactically acquainted with the use of the software and the practical application of *FEM*. For the comparison of the approaches the major boundary conditions, i.e. the method of load application, contact zones, mesh settings and findings will be mentioned. As mentioned in chapter 1, the simulation is divided into two load steps. During the first load step the cable gets clamped between clamp and housing to obtain the form fit to realise the strain relief. During the second load step, instead of the adhering to the standard test routine, the cable is pulled out of the strain relief module with a single pull to measure the maximum applicable tangential force F_x for the specific tooth geometry before sliding occurs.

Initial Simulation Concepts

The first noteworthy model is already reduced to the essential localities and takes advantage of the local symmetry to reduce computation time. The behaviour of the *PVC-P* cable sheath is predicted by the hyperelastic *Neo-Hooke* material model. For the initial model the user's thumb pressing the clamp into the cable was translated as a *force* boundary condition acting on an area on the top of the clamp, while only vertical translation of the clamp was allowed. The three major contact zones are the contacts between housing and cable, clamp and cable and clamp an housing. Fig. 3.16 shows an overall cross sectional view of the model and its individual components. The half model has been extended to a full model for better visualisation. The connection between clamp and housing is well visible. After applying the thumb force the clamp end position of the first load step should be identical with our experimental findings as listed in Tab. 3.2. Unfortunately, the model never converged.

The adapted approach that followed was identical in terms of geometry but had a different way of load application. Instead of applying a force on the clamp surface, the clamp was moved to its end position of load step 1, introducing an initial penetration to the system which was formed out during the first load step. This means the cable sheath tries to press the clamp teeth out of the material while the clamp itself is fixed in the notch position resulting in the cable being pressed downwards into the teeth of the housing. This approach also failed to reach convergence.

Simplified Simulation Concept

The model was further simplified to reduce computation time and increase the overall robustness so the simulation would run successfully. The simulation is now *displacement* driven, meaning the load application is introduced via the displacement of the clamp into the final notch position as part of the first load step, the contact between housing and clamp has been omitted and the cable core and wire insulation has been melted together with the cable sheath to create a single *PVC-P* cable body, see Fig. 3.17a and Fig. 3.17b. Additionally, fillets have been applied to the sharp edges and corners in the contact regions, see Fig. 3.17c. Furthermore, the mesh has been adapted several times so that regions with high deformations and stresses have a high resolution or a small element size. These areas are e.g. located at the cable surface as imprints of the geometry of the indenting body to keep the mesh element count manageable, see Fig. 3.17c. To counteract the high element distortions that nevertheless occur in the cable sheath a *Nonlinear Adaptive Region* was introduced for the sheath, which is an automatic feature that adapts the mesh during simulation based on certain criteria, e.g. element skewness [25]. This option was

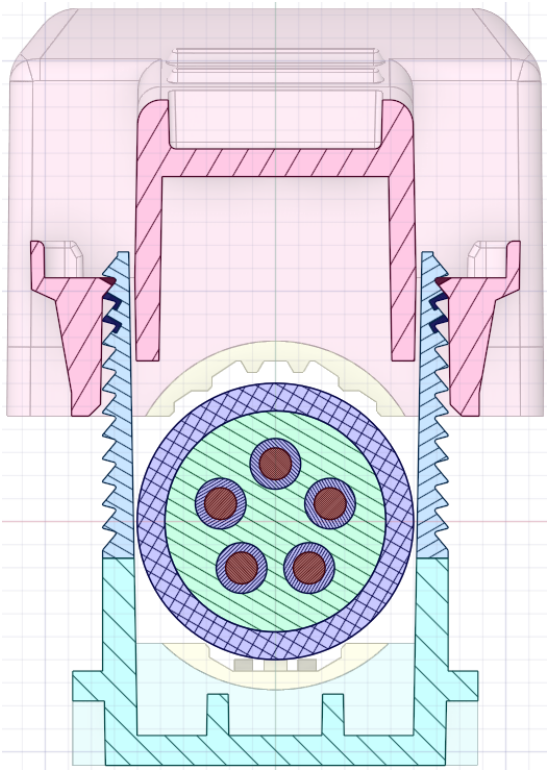

(a) Cross sectional view of the localized model before applying load

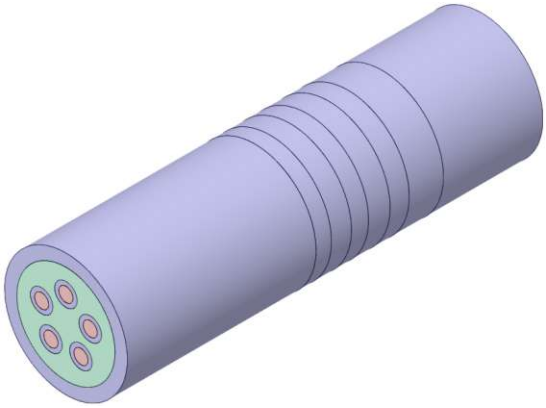

(b) Cable component with external surface split for simplified contact zone definition

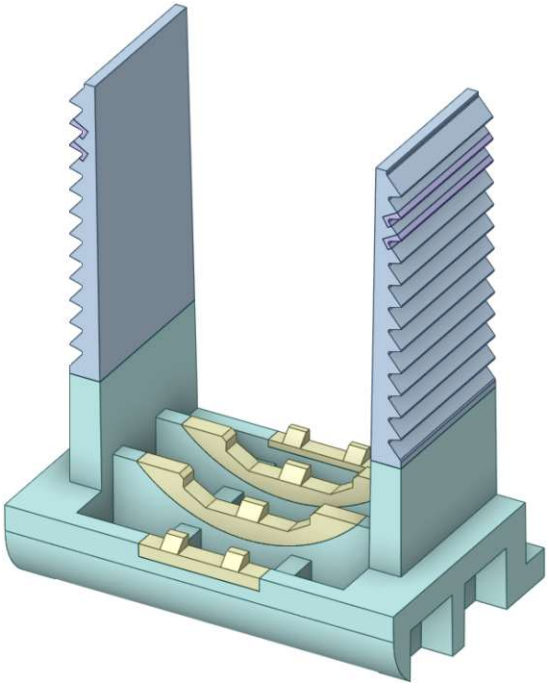

(c) Cut out section of housing bottom with detached bodies in contact region

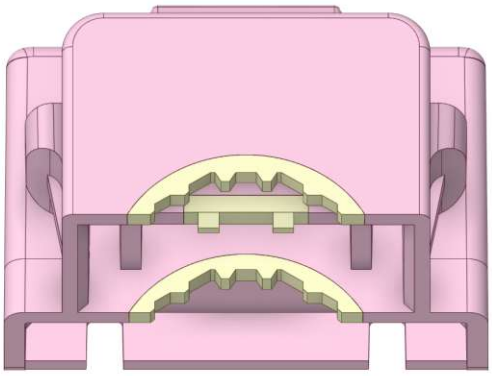

(d) View of clamp and its detached contact region bodies

Fig. 3.16: Overall view of an early simulation model and illustration of isolated components

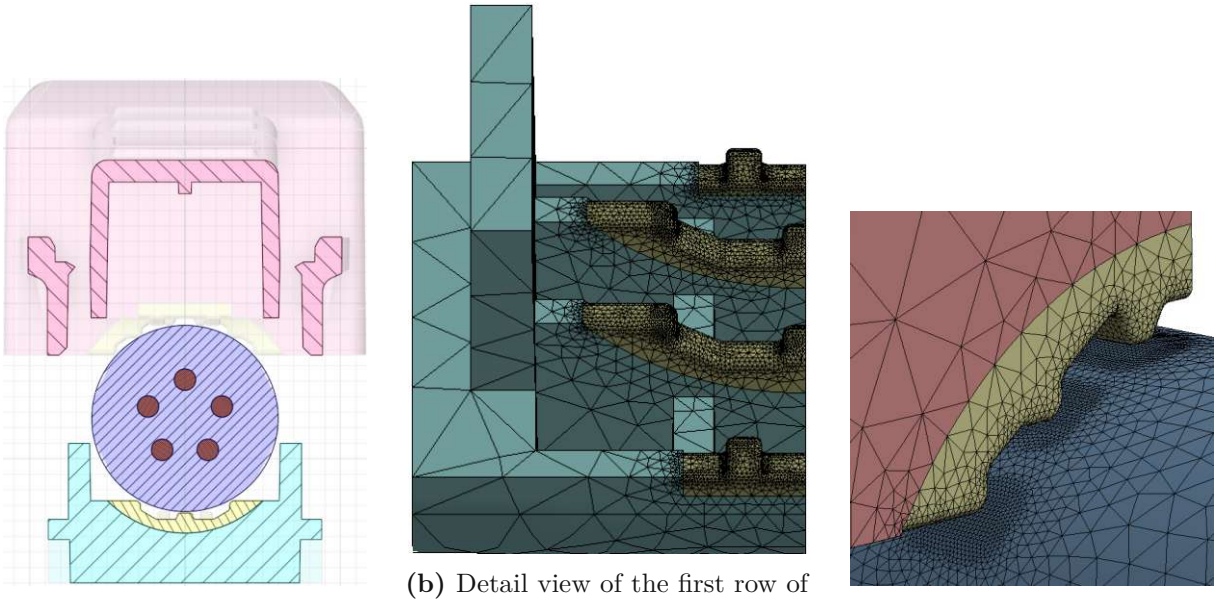

(a) Cross sectional view of the simplified model before applying load

(b) Detail view of the first row of teeth of the clamp and the cable surface with the mesh structure

(c) View of simplified housing bottom with mesh structure

Fig. 3.17: Selected detail views of the simplified and adapted simulation model

only used for a limited time, as its requirements and limitations outweighed its usefulness later on.

This approach led to a converging first load step for several simulation models of the different cable types as listed in Tab. 3.2, but not for the two top listed cable types, *H05VV-U5G1.5* and *H05VV5x2.5U*. In addition, the behaviour between the copper wires and the fused cable body was unsatisfactory as the possibility of relative movement between the cable innards and the sheath was omitted, which turned out to be a step into the wrong direction while applying the pull-out force during the second load step. At this point preparations for the calibration of the *TN*-model began.

Final Simulation Concept

After calibrating and applying the *TN*-model, overall convergence was reached and the reintroduction of complexity to the model was started, e.g. remodelling the cable and splitting the *PVCs*. For the second load step clamping jaws were added to realistically apply the pull-out force, see Fig. 3.18a. They clamp the cable at a standard conforming distance, see chapter 1, with a *rough* contact setting which corresponds to an infinite friction coefficient between the contacting bodies and prevents sliding. Furthermore, the cable was lengthened to accommodate the extra space needed for the jaws, resulting in a larger number of mesh elements, which was compensated

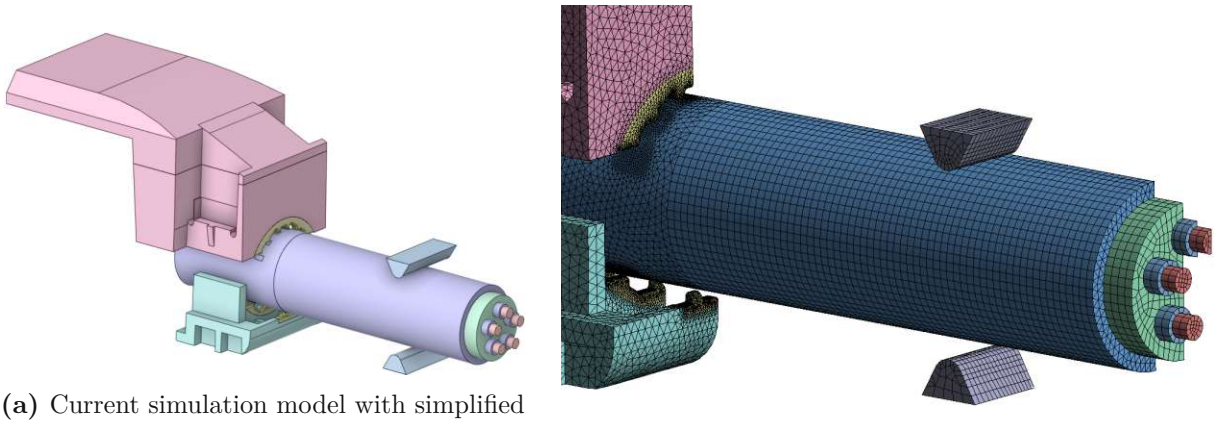

(a) Current simulation model with simplified clamp and clamping jaws for the second load step

(b) Detail view to show the hexahedra dominant cable mesh

Fig. 3.18: Representation of the latest simulation model with the original indentation geometry

for by a further adjustment of the mesh leading to a cable mesh in which hexahedron elements dominate while tetrahedra are only used where the indentation takes place, since they are more prone to erroneous element distortion. The body elongation or deformation is greatest at the outer cable sheath directly at the contact zones and decreases up to the copper wires to be practically zero there. Therefore a stepped protrusion was modelled so that the corner mesh elements don't penetrate each other when sliding over the edges of the bodies, see Fig. 3.18b. In contrast, the relative body displacement behaves in exactly the opposite way – as the cable sheath is clamped, the copper experiences the highest displacement. Although the displacement due to elongation is greater than the relative body movement, one could say, the cable innards are being pulled out of the sheath.

3.3.2.2 Model Comparison

For the final evaluation, the systems with the original, truncated pyramid and cone shaped teeth and the *H05VV-U5G1.5* cable are compared in regards to the *functionality*, *usability*, the maximum sliding distance at the contact zones and the resulting stresses. Using the final simulation concept, the cone and pyramid model were compared. The models differed in the actual tooth geometry and their height – the truncated cone is taller than the pyramid with 0.6 mm from bottom to top – which means, reaching the same notch position results into different vertical displacements. During the second load step the clamping jaw experiences a tangential translation of 2.7 mm, which is the maximal translation at which convergence was still achieved across all models.

Tab. 3.9: Final *FEA* results for the half models

Model	F_{xmax} [N]	F_{Nmax} [N]	F_x/F_N	$F_{xi}/F_{xmaxglobal}$	Value	Displacement [mm]
Original	82.38	79.67	1.03	0.955	0.993	1.902
Cone	85.35	88.57	0.964	0.993	0.981	2.163
Pyramid	85.96	84.64	1.016	1.000	1.006	1.9613

Tab. 3.10: F_{xi} and F_{Ni} of the full models and the ratio to the experimentally applied 120N thumb force

Model	F_{xfull} [N]	F_{Nfull} [N]	F_{Nfull}/F_{thumb} [%]
Original	164.76	159.34	32.78
Cone	170.35	177.14	47.62
Pyramid	171.9	169.28	41.07

Tab. 3.9 shows the results of the previously mentioned metrics of the half models. To obtain the forces acting on the full model these values have to be doubled, see Tab. 3.10. One can see, that the *displacement* corresponding forces F_{Nfull} exceed the previously chosen maximum thumb force. The differentiation between the *value* of the different models is below 3 % with the pyramid model performing best, ahead of the original and the cone model. Furthermore, the cone model has a greater normal force F_N of over 11 % compared to the original model and about 5 % compared to the pyramid model, which can be explained with the greater vertical displacement of the clamp in the cone model. The tangential or retention force F_x is about the same for the cone and pyramid model while the original model has around 4 % less. The cone model seems to prevent the cable from sliding the best, see Tab. 3.11, as the maximum sliding distance at the contact zones is more than a third smaller than the original and the pyramid model, while the difference between the original and the pyramid is only marginal.

Fig. 3.19 shows the von Mises stresses in the strain relief components, i.e. the clamp and the housing. The stress distribution of the original model, see Fig. 3.19a, shows a maximum stress of 62.54 MPa at the front tooth flank. It can be seen, that stresses in the cone model are the lowest, see Fig. 3.19b, having a maximum of 58.32 MPa at the front taper, while the stresses in the pyramid model are the highest with a maximum of 65.16 MPa, see Fig. 3.19c, concentrated on the pyramid flanks and, in contrast to the other models, especially at the rear part of the strain relief. All the stresses are below the yield stress of Makrolon 2467 at 66 MPa. The stress in the pyramid model is very close, but it's still almost 10 % short of the fracture stress of the material at 70 MPa.

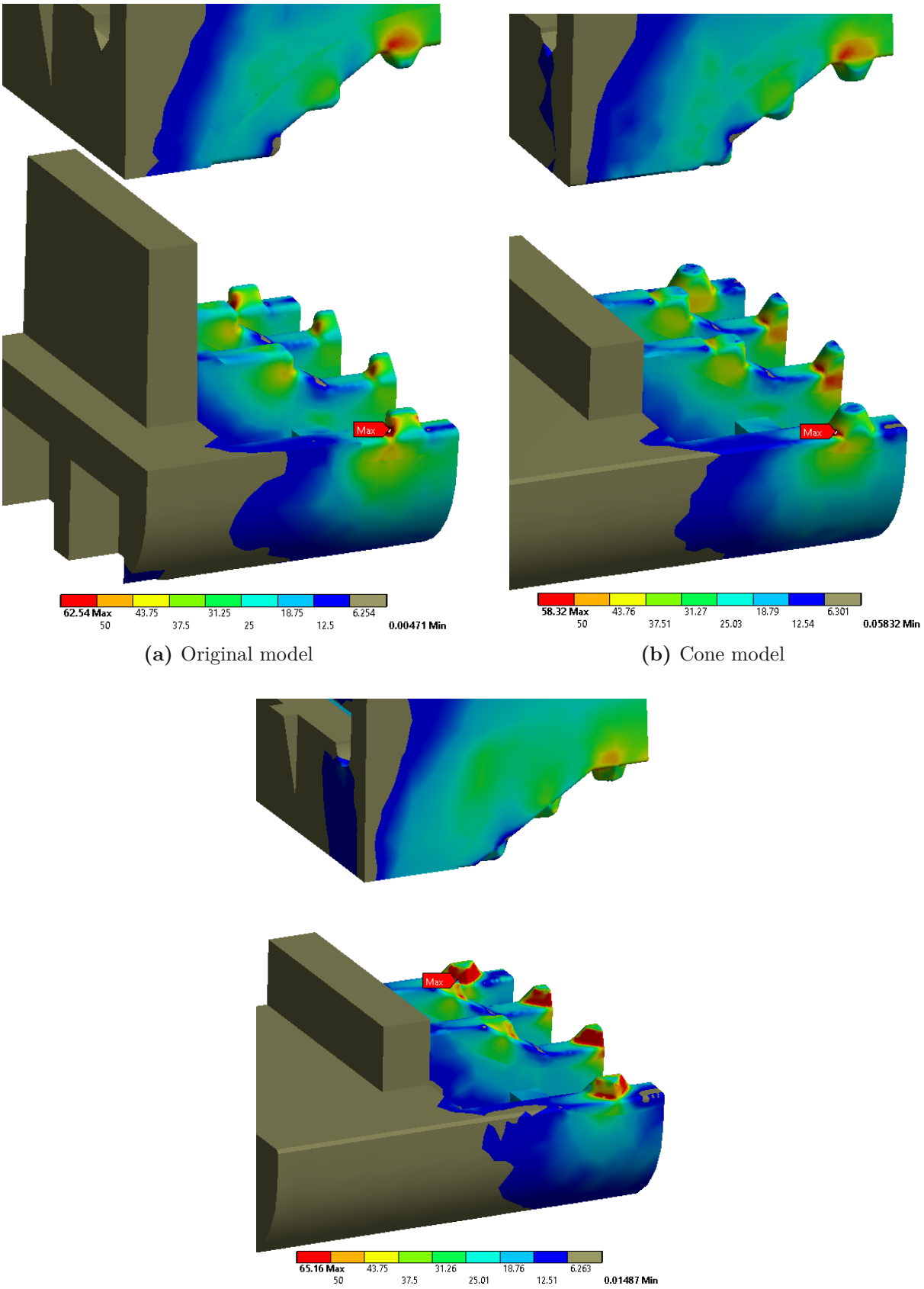

(a) Original model

(b) Cone model

(c) Pyramid model

Fig. 3.19: Detail views of the von Mises stresses in the strain relief components at the end of the second load step

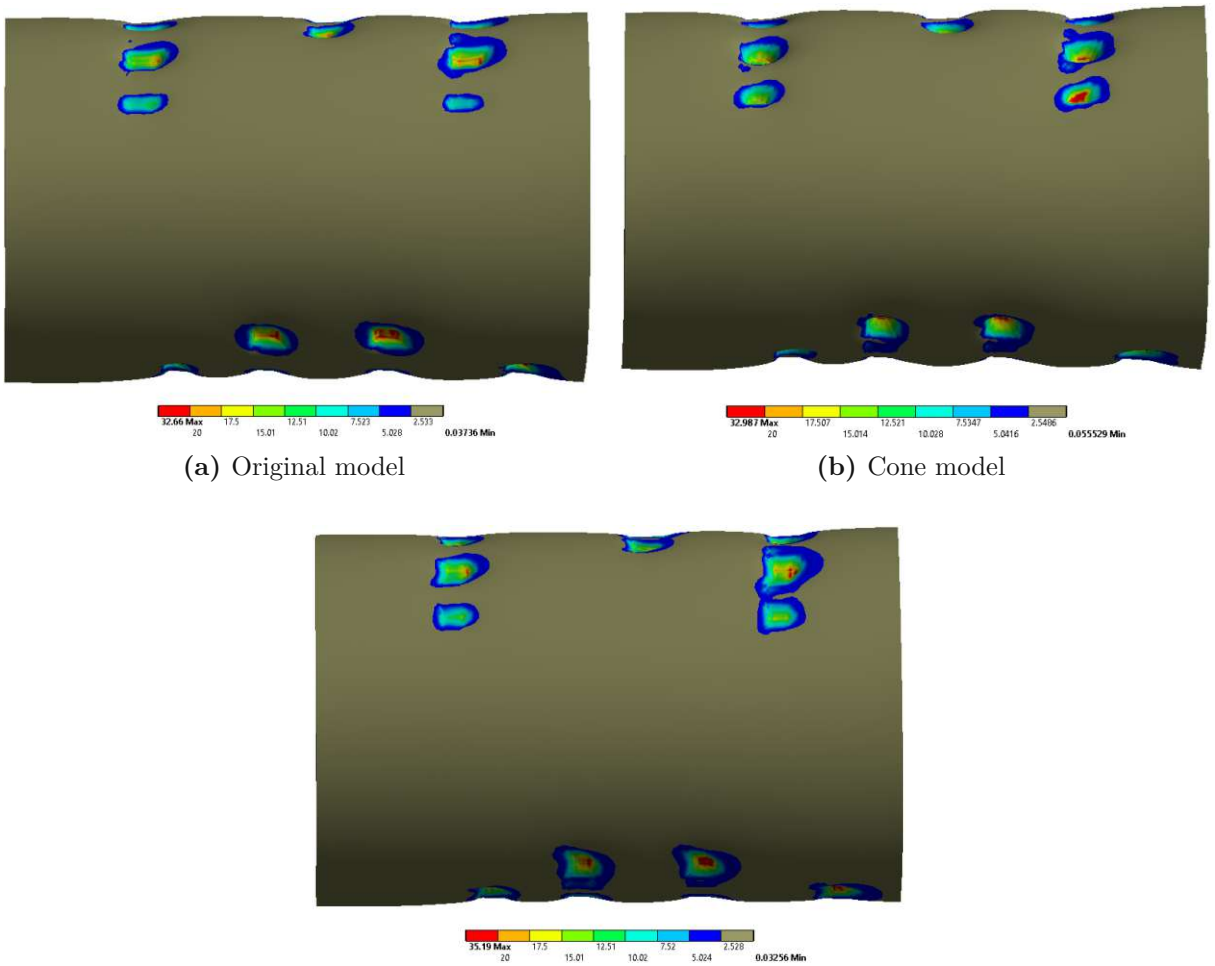

(a) Original model

(b) Cone model

(c) Pyramid model

Fig. 3.20: Detail views of the von Mises stresses in the cable sheath at the end of the second load step

Tab. 3.11: Maximum stress values and sliding distances occurring in the different simulation models

Model	Max Stress *PC* [MPa]	Max Stress *PVC* [MPa]	Sliding Distance [mm]
Original	62.54	32.66	0.401
Cone	58.32	32.99	0.295
Pyramid	65.16	35.19	0.393

Looking at the stress distribution in the cable sheath, see Fig. 3.20, we see that the lowest maximum stress is registered in the original model at 32.66 MPa followed by the cone model with a marginally greater value of 32.99 MPa and the pyramid model with an almost 10 % higher value of 35.19 MPa compared to the original model. Tab. 3.11 shows the maximum stresses occurring in the respective models in a clear manner.

Chapter 4

Discussion & Outlook

In the following pages we will discuss the results of the experiments, optimisation algorithm, the material model calibration and the simulation model comparison *FEAs*.

4.1 Experiments

We shall have another look on the material parameter determining experiments. While in the end we finally received material plates of the actual *PVC-P* material used for the cable sheathing from the international manufacturer which opened the possibility of calibrating a more sophisticated material model, the plates were fairly miniaturised and further processing of the material into proper experiment specimen proved to be difficult. For example, the plane strain tension or simple shear experiments had to be omitted, as the plates were too small, which led to the calibration with only two loading modes, tension and compression.

Furthermore, the experiments were conducted in a material sciences laboratory at the Vorarlberg University of Applied Sciences, which is meant to teach students the basics of deformation and fracture mechanics. Although there is a high level of experience with material testing for industry, the machinery and resources are not at the level of professional materials laboratories, especially for elastomer testing. E.g. the specimen weren't cured before testing and neither the temperature or the humidity were controllable parameters.

A later discussion with Dr. Jorgen Bergström revealed the possibility of friction polluting the compression data, since the measured asymmetry between tension and compression is unusual. Although the compression specimen were lubricated before carrying out the experiments, it was not checked whether the lubricant was suitable regarding the chemical compositions of the materials involved.

To further improve the quality of the experimental data, the cable manufacturer should be urged to provide larger sheets of material so that the processing of proper experiment specimen is possible and the experiments should be carried out in a professional elastomer laboratory.

4.2 Material Model

The material model would benefit greatly from improved quality of the experimental data, especially with the addition of shear stress data. The inconsistency between material behaviour prediction (*MCalibration*) and measurement (*Ansys*) lead to countless model adaptations and validation attempts and culminated in a discussion with *MCalibration* developer Dr. Bergström, resulting in the identification of possible experimental flaws. Dr. Bergström supposedly succeeded in validating the *MCalibration* material model with the *Ansys* solver inside the *MCalibration* application itself – using different solvers inside the application is a feature of the software – without significant problems. However, this could not be reproduced by the author.

The possibility exists that the experiment simulations were modelled erroneously and the subsequent adjustment of the material parameters was not correct and led to further degradation of the model. But as far as the measured data shows, the material model quality improved. In that case, validating the experiment simulation routine would be a logical next step and could bring clarity to this issue. Furthermore, calibrating the model using another method, e.g. a different software, could also lead to valuable additional information.

Some astute readers will be wondering about the status of the *Neo-Hooke* material model, which they read about briefly in the first few pages of this work. In fact, compared to its successor, the *TN-model*, it behaved very poorly and was way off at predicting the material behaviour, that's why it wasn't mentioned later on. But at the time, where nothing else was available it was sufficient.

4.3 Optimisation

Revisiting the optimisation process and its results after the *FEAs* we can see that if we compare the data from Tab. 3.2, 3.4, 3.6, 3.7 and 3.9, the optimisation predicted ratio between tangential and normal force F_x/F_N which lies between 46–59 % is off the actual measured virtual and experimental ratios. Rather, it appears that the *MDR* results are almost solely based on frictional forces, since the chosen coefficient of friction is $\mu = 0.52$ and the ratios F_x/F_N correlate with it,

while in reality the form fit due to the rubber-like behaviour has a major share in the overall result. A plausible reason for that is the mentioned assumptions and simplifications which preceded the optimisation process. The optimisation using *MDR* was always seen as a support activity for making qualitative statements and decisions regarding design choices rather than a mean to obtain quantitative results. If quantitative results are desired, one must extend the algorithm and include the viscoplastic material behaviour, see [18, 31, 33], account for the adhesive forces which play a considerable role in rubber friction [53] and extend the method to arbitrary, non-isolated profiles, see [54]. But even then, it seems unlikely to get meaningful, quantitative results given the complexity of the problem.

4.4 *FEA* Results

First of all, various simplifications and result affecting influences should be made clear to the reader. The following measures simplified and accelerated the simulation process, but probably also introduced possible sources of error and led to a deviation of the results. The initial goal of the project was to fully simulate the standardised tests of cable strain relief components of *LED* driver housings to help the development engineer validate critical design choices before ordering expensive injection moulding tools and performing the actual tests. Ultimately, the simulations carried out were not as extensive as the standard test, as it was decided that assessing the effects of a single high force pull was sufficient to extrapolate and predict the behaviour of a series of successive pulls, saving time and computing resources. We assumed that if the system behaves favourably over another after the first pull, it will continue to do so for x number of consecutive pulls.

The final simulation models were built around one cable type in a specific arrangement, which allowed the model to be split in the symmetry plane and saved significant resources, but also prevented the simulation of cable misalignment situations, including the alignment of the copper wires inside the cable. Although the standardised tests are carried out by experts in laboratories where cable misalignments are unlikely to occur, imperfect cable installations will happen outside the laboratories and should be tested on a full simulation model in future research. Due to limited resources the other relevant cable types, see Tab. 3.2, were excluded from further simulations as was the variability in cable diameter, but the systems ability of handling these tasks has been made evident with previous simulations, as mentioned in chapter 2, and adapting the latest simulation approach to fit these cable variations should be a manageable task.

By omitting the notched component of the housing intended for locking the clamp position, the system has been stiffened. Earlier simulations have shown that the force acting against the cable deformation causes these components to bend, resulting in a small displacement of the clamp itself, which reduces the final total normal force experienced by the clamp. In terms of the aforementioned reintroduction of complexity into the system, adding these components and their contacts to the model brings the simulation closer to reality.

Evaluating the isolated tooth *3D FEA* results in Tab. 3.7 and the final *FEA* results of Tab. 3.9 in regards to the mentioned non-axisymmetric research in chapter 2, one could say that the normal stiffness increasing nature of shapes with a lower polygonal order cross section leads to especially high normal or tangential forces, as the triangular pyramid scores well on these criteria in all the *FEA* comparisons, although the pyramidal shape had to be adapted to conform with the geometrical constraints. This is not surprising as the direct proportionality of F_N to normal stiffness and F_x to F_N is known, see Eq. 2.9 and 2.17.

The mentioned material model problems obviously introduced significant result deviating influences. A qualitative comparison between the different models of the same approach is indeed possible and can likely be interpreted for successful future design choices, but with the current state of the material model, force and stress results are estimated to deviate by up to 50% as tensile loading gets over predicted and the compressive loading under predicted, so the results should not be relied on exclusively. The ratio F_{Ni} to thumb force is shown in Tab. 3.10 and can be seen as an indication of the material model quality or, more fittingly, as a measure of error. For quantitative statements, this error should be reduced as much as possible, but at least below 10%.

We analyse and try to interpret the maximum stresses occurring in the models, see. Tab. 3.11 and Fig. 3.19 and 3.20, knowing that the values deviate by at least one third to one half from the experimental values. Since we know that the value of the normal force is inflated, it is likely that this also applies to the stresses. The stresses of the *PC* components are not critical in any of the models even with the overly stiff material model, meaning the clamp and housing are handling the load very well without the onset of yielding or breaking, which corresponds to the observations made during the pull-out experiments. On the other hand, all the *PVC* cable sheaths experienced surface scratching during the same experiments. This leads to the hypothesis that for proper failure prediction a damage and failure model is practical. The *Parallel*

Network (*PN*) is an extension of the *TNM* and its framework supports different damage and failure models [24], but it is currently not implemented in *Ansys* and one would have to add it with a workaround, e.g. an *Ansys Parametric Design Language* (*APDL*) command snippet. As mentioned in Sec. 2.3.4, different criteria are used to describe the point at which a material yields or breaks, but easy applicable phenomenological models are not practical for polymers and micromechanical models are very complex. If it is decided that a damage model is to be calibrated one must overcome the complexity. As a practical intermediate step or manageable alternative, a precise material model is needed to exactly copy the pull-out experiments and analyse the local load distribution at the point of failure to gain insights of the critical load and possibly translate it to Mises stresses for the time being. Using this information allows for local failure prediction when the critical stresses are reached. On the other hand, we know that surface damage doesn't occur during the standardised test procedures – the standardised cyclic tangential forces are lower than the forces applied in the pull-out tests – thus spending resources on the additional definition of a damage model might not be necessary to achieve the initial goal of fully simulating the standardised tests of the cable strain relief components. However, in order to achieve reliable results in these simulations, the material model must be optimised as already mentioned.

Coming back to the resulting stress distribution for the cable sheath, comparing Tab. 3.2 and 3.10, we know that in reality local material failure and surface scratching occurs at a pull-out force of about 131 N, while in the simulation we assume the force to be one third to one half higher due to the material model stiffness, i.e. between 173–195 N, which barely is reached in the cone and pyramid model for the chosen tangential cable displacement of the final simulation. Nonetheless, we can deduct some qualitative statements including the results from Tab. 3.11. First of all, the amount of vertical clamp displacement and the $F_{N\,full}/F_{thumb}$ ratio are directly proportional. The highest displacements and ratios are registered for the cone model, compared to the original model it has a 13.7% larger displacement and a 45.3% larger ratio, which correlates with our finding that the prediction of the material model has a larger deviation at higher strains. Taking the results of the pyramid model into account, the proportionality does not seem to be linear – we have a non-linear material model after all. If we examine F_x/F_N and $F_{xi}/F_{xmaxglobal}$ or otherwise defined as *usability* and *functionality* in isolation – which basically corresponds to the *value* – the final results are not as conclusive as expected, after the pyramid model clearly prevailed in the *3D FEA* tooth shape comparison and the cone model performed significantly better than the original one, see. Tab. 3.7. The differences are only marginal. It is clear, that relying solely on

those metrics isn't enough. One must also include the probability of material failure, as we know that this is associated with loss of function, and the contact zone sliding, as this must be kept at a minimum and isn't allowed to reach the 2 mm threshold. For future research, it is probably interesting to find the sweet spot between these two constraints. The pyramid model achieved the highest *value* of the three models, but it also registered the highest maximum stresses in the cable sheath, almost 10% higher than the other models, meaning material failure is probable to occur first in this model. In addition, the sliding of the cable was only marginally less than in the original model, in which, however, the cable slid significantly further than in the cone model, namely by about a third. Across the board, the cone model performs best or very close to it in all of the criteria of Tab. 3.11. Regarding the stress distributions the cone model seems to be particularly well balanced, because although it experienced the highest vertical clamp displacement, it still recorded the lowest maximum stresses and also the highest average stress in the contact zones, which might be an indicator for a well distributed load and thus a reason for the low sliding distance. Also, the comparatively low maximum stresses in the clamp and housing of the cone model lead to less deformation of the *PC* components, which results in a firmer hold of the cable. All in all, the *3D FEA* results are still not overwhelmingly in favour of any of the models, but the cone model appears to be an improvement over the others. Additionally it showed the highest tangential forces when applying the *MDR* transformation during the optimisation phase. The author therefore recommends this model for further prototypical test procedures. For future research, a virtual comparison of the different models with equal vertical clamp displacement and a laboratory test of the different models via rapid prototyping would be interesting.

Furthermore, to immensely increase the complexity the geometric constraint of sticking to the initial tooth positions or the clamp and housing design could be omitted and replaced by a spatial constraint, limiting only the most critical dimensions of the components. Paired with generative design [55], this could help find better solutions and lead to less conventional design choices [56].

In conclusion, the development or optimisation approach outlined in this work and its models can be used by design engineers at many stages of the product development cycle of a polycarbonate component, especially in combination with plasticised polyvinyl chloride components, but with some limitations until further material model refinements are made. Example activities include the evaluation of active principles, testing and comparing design options or optimising existing

structures, as was done for the use case presented in this work, and the validation of functionality.

Bibliography

[1] S. Vajna, C. Weber, K. Zeman, P. Hehenberger, D. Gerhard, and S. Wartzack. *CAx für Ingenieure: eine praxisbezogene Einführung*. 3., vollständig neu bearbeitete Auflage. Berlin, Germany: Springer Vieweg, 2018. 655 pp. ISBN: 978-3-662-54623-9. DOI: 10.1007/978-3-662-54624-6.

[2] G. Dhatt, G. Touzot, E. Lefrançois, and P. Breitkopf. *Finite element method*. eng. Numerical methods series. London : Hoboken, N.J. :John Wiley and Sons Inc.: ISTE Ltd. ; 2012. ISBN: 1118569768.

[3] C. Lo, C. Chen, and R. Y. Zhong. "A review of digital twin in product design and development". en. In: *Advanced Engineering Informatics* 48 (Apr. 2021), p. 101297. ISSN: 14740346. DOI: 10.1016/j.aei.2021.101297. URL: https://linkinghub.elsevier.com/retrieve/pii/S1474034621000513 (Accessed on 02/09/2022).

[4] M. S. Shephard, M. W. Beall, R. M. O'Bara, and B. E. Webster. "Toward Simulation-Based Design". In: *Finite Elem. Anal. Des.* 40.12 (July 2004), pp. 1575–1598. ISSN: 0168-874X. DOI: 10.1016/j.finel.2003.11.004. URL: https://doi.org/10.1016/j.finel.2003.11.004.

[5] P. Kestel, T. Schneyer, and S. Wartzack. "Feature-Based Approach for the Automated Setup of Accurate, Design-Accompanying Finite Element Analyses". In: 2016.

[6] C. Carro Saavedra, N. J. Marahrens, S. Schweigert, P. Kestel, S. Kremer, S. Wartzack, and U. Lindemann. "Development of a toolkit of methods for simulations in product development". In: *2016 IEEE International Conference on Industrial Engineering and Engineering Management (IEEM)*. 2016, pp. 631–635. DOI: 10.1109/IEEM.2016.7797952.

[7] *OVE EN IEC 60598-1, Luminaires – Part 1: General requirements and tests*. Tech. rep. OVE Österreichischer Verband für Elektrotechnik. URL: https://shop.ove.at/de/product/ove-en-60598-1-a2-2019-07-15 (Accessed on 03/31/2023).

[8] D. Kazmer. *Injection Mold Design Engineering*. Carl Hanser Verlag GmbH & Company KG, 2022. ISBN: 978-1-56990-892-1. URL: https://books.google.at/books?id=xbaREAAAQBAJ.

[9] M. P. Bendsøe and O. Sigmund. *Topology optimization: theory, methods, and applications*. Berlin ; New York: Springer, 2003. ISBN: 978-3-540-42992-0.

[10] E. Andreassen, A. Clausen, M. Schevenels, B. S. Lazarov, and O. Sigmund. "Efficient topology optimization in MATLAB using 88 lines of code". en. In: *Structural and Multidisciplinary Optimization* 43.1 (Jan. 2011), pp. 1–16. ISSN: 1615-147X, 1615-1488. DOI: 10.1007/s00158-010-0594-7. URL: http://link.springer.com/10.1007/s00158-010-0594-7 (Accessed on 04/07/2023).

[11] O. Sigmund and K. Maute. "Topology optimization approaches". In: *Structural and Multidisciplinary Optimization* 48.6 (Dec. 2013), pp. 1031–1055. ISSN: 1615-1488. DOI: 10.1007/s00158-013-0978-6. URL: https://doi.org/10.1007/s00158-013-0978-6.

[12] M. Stolpe. "Truss optimization with discrete design variables: a critical review". In: *Structural and Multidisciplinary Optimization* 53.2 (Feb. 2016), pp. 349–374. ISSN: 1615-1488. DOI: 10.1007/s00158-015-1333-x. URL: https://doi.org/10.1007/s00158-015-1333-x.

[13] Z. Shuai, D. Sier, Z. Wenhu, and K. Naizheng. "Simulation and experiment on sealing mechanism with rigid-flexible combined seal groove in hub bearing". In: *Tribology International* 136 (2019), pp. 385–394. ISSN: 0301-679X. DOI: https://doi.org/10.1016/j.triboint.2019.04.005. URL: https://www.sciencedirect.com/science/article/pii/S0301679X19301999.

[14] M. Achenbach. "Service life of seals – numerical simulation in sealing technology enhances prognoses". In: *Computational Materials Science* 19.1 (2000), pp. 213–222. ISSN: 0927-0256. DOI: https://doi.org/10.1016/S0927-0256(00)00157-9. URL: https://www.sciencedirect.com/science/article/pii/S0927025600001579.

[15] L. Etman, D. van Campen, and A. Schoofs. "Design Optimization of Multibody Systems by Sequential Approximation". In: *Multibody System Dynamics* 2.4 (Dec. 1998), pp. 393–415. ISSN: 1573-272X. DOI: 10.1023/A:1009780119839. URL: https://doi.org/10.1023/A:1009780119839.

[16] C. L. Bottasso, F. Campagnolo, A. Croce, S. Dilli, F. Gualdoni, and M. B. Nielsen. "Structural optimization of wind turbine rotor blades by multilevel sectional/multibody/3D-FEM analysis". en. In: *Multibody System Dynamics* 32.1 (June 2014), pp. 87–116. ISSN: 1384-5640, 1573-272X. DOI: 10.1007/s11044-013-9394-3. URL: http://link.springer.com/10.1007/s11044-013-9394-3 (Accessed on 04/07/2023).

[17] D. Sarojini and D. N. Mavris. "Structural Analysis and Optimization of Aircraft Wings Through Dimensional Reduction". PhD thesis. May 2021. URL: http://hdl.handle.net/1853/64716.

[18] V. Popov, M. Heß, and E. Willert. *Method of Dimensionality Reduction in Contact Mechanics: User's Manual*. Aug. 2018. ISBN: 978-3-00-060382-2.

[19] C. Mattheck. *Design in nature: learning from trees*. eng. Berlin; New York: Springer-Verlag, 1998. ISBN: 978-3-540-62937-5.

[20] R. W. Hertzberg, R. P. Vinci, and J. L. Hertzberg. *Deformation and fracture mechanics of engineering materials*. Fifth edition. Hoboken, NJ: John Wiley & Sons, Inc, 2012. ISBN: 978-0-470-52780-1.

[21] K. Papailiou. "On the bending stiffness of transmission line conductors". In: *IEEE Transactions on Power Delivery* 12.4 (1997), pp. 1576–1588. DOI: 10.1109/61.634178.

[22] K. Spak, G. Agnes, and D. Inman. "Parameters for Modeling Stranded Cables as Structural Beams". In: *Experimental Mechanics* 54.9 (Nov. 2014), pp. 1613–1626. ISSN: 0014-4851, 1741-2765. DOI: 10.1007/s11340-014-9941-8. URL: http://link.springer.com/10.1007/s11340-014-9941-8 (Accessed on 09/23/2022).

[23] *Makrolon® 2467*. Covestro AG. Sept. 23, 2022. URL: https://solutions.covestro.com/de/products/makrolon/makrolon-2467_56977450-00003066?SelectedCountry=AT.

[24] J. S. Bergstrom. *Mechanics of Solid Polymers: Theory and Computational Modeling*. eng. First edition. The PDL handbook series. Norwich: Elsevier Science & Technology Books, 2015. ISBN: 9780323311502.

[25] *Mechanical User's Guide*. English. Version 2022 R2. Ansys, Inc. Canonsburg, USA, July 2022. 2570 pp. URL: http://www.ansys.com.

[26] W. Rust. *Nichtlineare Finite-Elemente-Berechnungen mit ANSYS Workbench: Strukturmechanik: Kontakt, Material, große Verformungen*. ger. 1st ed. 2020. Wiesbaden: Springer Fachmedien Wiesbaden Imprint: Springer Vieweg, 2020. ISBN: 3658314214. URL: 10.1007/978-3-658-31421-7.

[27] J. Barber. *Contact Mechanics*. Vol. 250. Solid Mechanics and Its Applications. Cham: Springer International Publishing, 2018. ISBN: 978-3-319-70938-3 978-3-319-70939-0. DOI: 10.1007/978-3-319-70939-0. URL: http://link.springer.com/10.1007/978-3-319-70939-0 (Accessed on 08/21/2022).

[28] *Optimization*. Aug. 29, 2022. URL: https://www.merriam-webster.com/dictionary/optimization.

[29] A. Schumacher. *Optimierung mechanischer Strukturen: Grundlagen und industrielle Anwendungen*. ger. 3rd ed. 2020. Berlin Heidelberg: Springer Berlin Heidelberg Imprint: Springer Vieweg, 2020. ISBN: 3662603284. URL: 10.1007/978-3-662-60328-4.

[30] J. Nocedal and S. J. Wright. *Numerical optimization*. eng. 2. ed. Springer series in operations research and financial engineering. New York, NY: Springer, 2006. ISBN: 0387303030.

[31] V. L. Popov and M. Heß. *Methode der Dimensionsreduktion in Kontaktmechanik und Reibung*. Berlin, Heidelberg: Springer Berlin Heidelberg, 2013. ISBN: 978-3-642-32672-1 978-3-642-32673-8. DOI: 10.1007/978-3-642-32673-8. URL: http://link.springer.com/10.1007/978-3-642-32673-8 (Accessed on 09/01/2022).

[32] V. L. Popov and M. Heß. *Method of Dimensionality Reduction in Contact Mechanics and Friction*. en. Berlin, Heidelberg: Springer Berlin Heidelberg, 2015. ISBN: 978-3-642-53875-9 978-3-642-53876-6. DOI: 10.1007/978-3-642-53876-6. URL: http://link.springer.com/10.1007/978-3-642-53876-6 (Accessed on 10/05/2022).

[33] V. L. Popov, M. Heß, and E. Willert. *Handbook of Contact Mechanics: Exact Solutions of Axisymmetric Contact Problems*. Berlin, Heidelberg: Springer Berlin Heidelberg, 2019. ISBN: 978-3-662-58708-9 978-3-662-58709-6. DOI: 10.1007/978-3-662-58709-6. URL: http://link.springer.com/10.1007/978-3-662-58709-6 (Accessed on 08/21/2022).

[34] V. L. Popov. "An Approximate Solution for the Contact Problem of Profiles Slightly Deviating from Axial Symmetry". In: *Symmetry* 14.2 (2022). ISSN: 2073-8994. DOI: 10.3390/sym14020390. URL: https://www.mdpi.com/2073-8994/14/2/390.

[35] V. L. Popov, R. Pohrt, and M. Heß. "General procedure for solution of contact problems under dynamic normal and tangential loading based on the known solution of normal contact problem". en. In: *The Journal of Strain Analysis for Engineering Design* 51.4 (May 2016), pp. 247–255. ISSN: 0309-3247, 2041-3130. DOI: 10.1177/0309324716632417. URL: http://journals.sagepub.com/doi/10.1177/0309324716632417 (Accessed on 08/21/2022).

[36] I. Lyashenko and V. Borysiuk. "The effects of half-space approximation and thickness of the contact bodies on the normal contact force: experiment and simulations". en. In: *Procedia Structural Integrity* 36 (2022), pp. 394–400. ISSN: 24523216. DOI: 10.1016/j.prostr.2022.01.051. URL: https://linkinghub.elsevier.com/retrieve/pii/S2452321622000592 (Accessed on 10/03/2022).

[37] R. King. "Elastic analysis of some punch problems for a layered medium". eng. In: *International journal of solids and structures* 23.12 (1987), pp. 1657–1664. ISSN: 0020-7683.

[38] Q. Li and V. L. Popov. "Indentation of flat-ended and tapered indenters with polygonal cross-sections". In: *Facta Universitatis, Series: Mechanical Engineering* 14.3 (Dec. 8, 2016), p. 241. ISSN: 2335-0164, 0354-2025. DOI: 10.22190/FUME1603241L. URL: http://casopisi.junis.ni.ac.rs/index.php/FUMechEng/article/view/2176 (Accessed on 08/21/2022).

[39] J. B. Pawley, ed. *Handbook Of Biological Confocal Microscopy*. en. Boston, MA: Springer US, 2006. ISBN: 978-0-387-25921-5 978-0-387-45524-2. DOI: 10.1007/978-0-387-45524-2. URL: http://link.springer.com/10.1007/978-0-387-45524-2 (Accessed on 10/07/2022).

[40] J. Bergstrom. *Smart Mechanical Testing of Polymers*. URL: https://polymerfem.com/smart-mechanical-testing-of-polymers/ (Accessed on 10/11/2022).

[41] *DIN EN ISO 527-1:2019-12, Kunststoffe – Bestimmung der Zugeigenschaften Teil 1: Allgemeine Grundsätze*. Tech. rep. Beuth Verlag GmbH. DOI: 10.31030/3059426. URL: https://www.beuth.de/de/-/-/306958894 (Accessed on 10/11/2022).

[42] *DIN EN ISO 527-2:2012-06, Kunststoffe – Bestimmung der Zugeigenschaften Teil 2: Prüfbedingungen für Form- und Extrusionsmassen*. Tech. rep. Beuth Verlag GmbH. DOI: 10.31030/1860304. URL: https://www.beuth.de/de/-/-/148232494 (Accessed on 10/11/2022).

[43] *DIN EN ISO 604:2003-12, Kunststoffe – Bestimmung von Druckeigenschaften*. Tech. rep. Beuth Verlag GmbH. DOI: 10.31030/9515267. URL: https://www.beuth.de/de/-/-/66571333 (Accessed on 10/11/2022).

[44] K. V. Shooter and D. Tabor. "The Frictional Properties of Plastics". In: *Proceedings of the Physical Society. Section B* 65.9 (Sept. 1, 1952), pp. 661–671. ISSN: 0370-1301. DOI: 10.1088/0370-1301/65/9/302. URL: https://iopscience.iop.org/article/10.1088/0370-1301/65/9/302 (Accessed on 08/21/2022).

[45] G. F. Moore and B. C. Ltd, eds. *Electric cables handbook*. 3rd ed. Oxford ; Malden, Mass: Blackwell Science, 1997. ISBN: 978-0-632-04075-9.

[46] Z.-M. Li and R. J. Goitz. "Biomechanical evaluation of the motor function of the thumb". In: *Technology and Health Care* 11.4 (Oct. 2003), pp. 233–243. ISSN: 09287329, 18787401. DOI: 10.3233/THC-2003-11403. URL: https://www.medra.org/servlet/aliasResolver?alias=iospress&doi=10.3233/THC-2003-11403 (Accessed on 10/13/2022).

[47] H. Brewer. "Yielding and Failure Criteria for Rubber Modified Polymers, Part 1". In: *Polymer Blends and Mixtures*. Ed. by D. J. Walsh, J. S. Higgins, and A. Maconnachie. Dordrecht: Springer Netherlands, 1985, pp. 375–382. ISBN: 978-94-009-5101-3. DOI: 10.1007/978-94-009-5101-3_19. URL: https://doi.org/10.1007/978-94-009-5101-3_19.

[48] T. L. Anderson. *Fracture mechanics: fundamentals and applications*. Fourth edition. Boca Raton: CRC Press/Taylor & Francis, 2017. ISBN: 978-1-4987-2813-3.

[49] S. K. Sinha, ed. *Handbook of polymer tribology*. Hackensack, New Jersey: World Scientific, 2018. ISBN: 978-981-322-778-1.

[50] A. J. Kinloch and R. J. Young. *Fracture Behaviour of Polymers*. en. Dordrecht: Springer Netherlands, 1995. ISBN: 978-94-017-1596-6 978-94-017-1594-2. DOI: 10.1007/978-94-017-1594-2. URL: http://link.springer.com/10.1007/978-94-017-1594-2 (Accessed on 03/30/2023).

[51] K.-F. Arndt and M. D. Lechner, eds. *Polymer Solids and Polymer Melts – Mechanical and Thermomechanical Properties of Polymers*. Berlin, Heidelberg: Springer Berlin Heidelberg, 2014. ISBN: 978-3-642-55165-9 978-3-642-55166-6. DOI: 10.1007/978-3-642-55166-6. URL: http://materials.springer.com/bp/docs/978-3-642-55166-6 (Accessed on 10/28/2022).

[52] I. N. Sneddon. "Boussinesq's problem for a rigid cone". In: *Mathematical Proceedings of the Cambridge Philosophical Society* 44.4 (1948), pp. 492–507. DOI: 10.1017/S0305004100024518.

[53] V. L. Popov. *Contact Mechanics and Friction*. en. Berlin, Heidelberg: Springer Berlin Heidelberg, 2017. ISBN: 978-3-662-53080-1 978-3-662-53081-8. DOI: 10.1007/978-3-662-53081-8. URL: http://link.springer.com/10.1007/978-3-662-53081-8 (Accessed on 03/23/2023).

[54] V. L. Popov, R. Pohrt, and M. Heß. "General procedure for solution of contact problems under dynamic normal and tangential loading based on the known solution of normal contact problem". In: *The Journal of Strain Analysis for Engineering Design* 51.4 (May 2016), pp. 247–255. ISSN: 0309-3247, 2041-3130. DOI: 10.1177/0309324716632417. URL: http://journals.sagepub.com/doi/10.1177/0309324716632417 (Accessed on 08/21/2022).

[55] M. McKnight. "Generative Design: What it is? How is it being used? Why it's a game changer". In: *KnE Engineering* 2.2 (Feb. 2017), p. 176. ISSN: 2518-6841. DOI: 10.18502/keg.v2i2.612. URL: http://knepublishing.com/index.php/KnE-Engineering/article/view/612/1903 (Accessed on 03/29/2023).

[56] D. Vlah, R. Žavbi, and N. Vukašinović. "Evaluation of Topology Optimization and Generative Design Tools as Support for Conceptual Design". In: *Proceedings of the Design Society: DESIGN Conference* 1 (2020), pp. 451–460. DOI: 10.1017/dsd.2020.165.

Appendix A

Julia Code Lines

The following code lines are defining the input used in all the different geometry optimisation algorithms:

```
### Importing necessary packages for optimisation##
using SpecialFunctions
using JuMP
import Ipopt

### Definition of input variables ###
E = 16.51        #MPa
d = 1.9202/2     #mm; indentation depth per side
tau_0 = 29.42    #MPa
eps = 1e-6       # auxilliary variable
mu = 0.52        # COF
G = 12.06        #MPa
u0=0.61          #mm
```

The next code lines are dependent on the geometry shape:

Cylinder

```
### Definition of profile specific functions ###
function FN_Cylinder(u0,E,d,a)
FN = 2*E*d*a
Fx = 2*G*a*u0
Fx,FN
end

### Definition of objective and constraints ###
obj(a)= FN_Cylinder(u0,E,d,a)[1]
FN(a)= FN_Cylinder(u0,E,d,a)[2]

Cylinder = Model(Ipopt.Optimizer)
register(Cylinder, :obj, 1, obj; autodiff = true)
register(Cylinder, :FN, 1, FN; autodiff = true)
@variable(Cylinder, 0 <= a <= 5)
@NLobjective(Cylinder, Max, obj(a))
@NLconstraint(Cylinder, FN(a)<=20)
optimize!(Cylinder)
```

```
@show termination_status(Cylinder)
@show primal_status(Cylinder)
@show dual_status(Cylinder)
@show objective_value(Cylinder)

### Output definition of optimised parameters ###
a_opt = value(a)
FN_opt= FN(a_opt)
Fx_opt = obj(a_opt)

C = Array{Any}(undef,1,3)
C[1,:] = [:Cylinder Fx_opt FN_opt]
```

Cylinder with Paraboloidal Cap

```
### Definition of profile specific functions ###
function FN_Cylinder_Paraboloid(a,c,d,E,G,mu,u0)
R = c^2/(d-u0*G/(mu*E))
FN = 2*E*(d*a-a^3/(3*R))
end

function Fx_Cylinder_Paraboloid(a,c,d,E,G,mu,u0)
R = c^2/(d-u0*G/(mu*E))
Fx = (2*mu*E)/(3*R)*((3*a*d*R)-a^3-2*c^3)
end

### Definition of objective and constraints ###
obj(a,c)= Fx_Cylinder_Paraboloid(a,c,d,E,G,mu,u0)
FN(a,c)= FN_Cylinder_Paraboloid(a,c,d,E,G,mu,u0)

Cylinder_Paraboloid = Model(Ipopt.Optimizer)
register(Cylinder_Paraboloid, :obj, 2, obj; autodiff = true)
register(Cylinder_Paraboloid, :FN, 2, FN; autodiff = true)
@variable(Cylinder_Paraboloid, 0 <= a <= 1)
@variable(Cylinder_Paraboloid, 0 <= c <= 1)
@NLobjective(Cylinder_Paraboloid, Max, obj(a,c))
@NLconstraint(Cylinder_Paraboloid, FN(a,c)<=20)
optimize!(Cylinder_Paraboloid)
@show termination_status(Cylinder_Paraboloid)
@show primal_status(Cylinder_Paraboloid)
@show dual_status(Cylinder_Paraboloid)
@show objective_value(Cylinder_Paraboloid)

### Output definition of optimised parameters ###
a_opt = value(a)
c_opt = value(c)
R_opt = c_opt^2/(d-u0*G/(mu*E))
FN_opt= FN(a_opt,c_opt)
```

```
Fx_opt = obj(a_opt,c_opt)

B = Array{Any}(undef,1,3)
B[1,:] = [:Cylinder_Paraboloid Fx_opt FN_opt]
```

Cone

```
### Definition of profile specific functions ###
function FN_Cone(d,E,G,a)
    c = a-2*G*u0/(pi*mu*E*(2*d/(pi*a)))
    FN = (pi*E*(2*d/(pi*a))*(a)^2)/2
    Fx = mu*FN*(1-c^2/a^2)
    Fx,FN,a,c
end

### Definition of objective and constraints ###
obj(a)= FN_Cone(d,E,G,a)[1]
FN(a)= FN_Cone(d,E,G,a)[2]

Cone = Model(Ipopt.Optimizer)
register(Cone, :obj, 1, obj; autodiff = true)
register(Cone, :FN, 1, FN; autodiff = true)
@variable(Cone, eps <= a <= 6)
@NLobjective(Cone, Max, obj(a))
@NLconstraint(Cone, FN(a)<=20)
optimize!(Cone)
@show termination_status(Cone)
@show primal_status(Cone)
@show dual_status(Cone)
@show objective_value(Cone)

### Output definition of optimised parameters ###
a_opt = value(a)
c_opt = a_opt-2*G*u0/(pi*mu*E*(2*d/(pi*a_opt)))
FN_opt= FN(a_opt)
Fx_opt = obj(a_opt)
theta_opt = atan(2*d/(pi*a_opt))*180/pi

C = Array{Any}(undef,1,3)
C[1,:] = [:Cone Fx_opt FN_opt]
```

Truncated Cone

```
### Definition of profile specific functions ###
function FN_Cone_cut(E,r,t,c,d)
    #t = d/(a*acos(b/a))
    # r = b/a
    # t = b/c
```

```
    # a = (t/r)*c
    FN = E*((t/r)*c*d+(r*c*sqrt(1-r^2)*d)/(acos(r)))
end

function Fx_Cone_cut(E,mu,r,t,c,d)
    Fx = (mu*E*d*c/((t/r)*acos(r)))
         *((t/r)^2*(acos(r) + r*sqrt(1-r^2)) - (r/t)*(acos(t)+ t*sqrt(1-t^2)))
end

### Definition of objective and constraints ###
obj(r,t,c)= Fx_Cone_cut(E,mu,r,t,c,d)
FN(r,t,c)= FN_Cone_cut(E,r,t,c,d)


Cone_cut = Model(Ipopt.Optimizer)
register(Cone_cut, :obj, 3, obj; autodiff = true)
register(Cone_cut, :FN, 3, FN; autodiff = true)
@variable(Cone_cut, eps <= r <= 1)
@variable(Cone_cut, eps <= t <= 1)
@variable(Cone_cut, eps <= c <= 5)
@NLobjective(Cone_cut, Max, obj(r,t,c))
@NLconstraint(Cone_cut, t <= (1-eps))
@NLconstraint(Cone_cut, r <= (1-eps))
@NLconstraint(Cone_cut, u0 >= mu*(E/G)*d*(1-((r/t)*acos(t)/acos(r))))
@NLconstraint(Cone_cut, FN(r,t,c) <= 20)
optimize!(Cone_cut)
@show termination_status(Cone_cut)
@show primal_status(Cone_cut)
@show dual_status(Cone_cut)
@show objective_value(Cone_cut)

### Output definition of optimised parameters ###
t_opt,r_opt,c_opt = value(t),value(r),value(c)
Fx_opt = obj(r_opt,t_opt,c_opt)
FN_opt = FN(r_opt,t_opt,c_opt)

a_opt = (t_opt/r_opt)*c_opt
b_opt = t_opt*c_opt

theta_opt = atan(d/(a_opt*acos(b_opt/a_opt)))*180/pi

 C = Array{Any}(undef,1,3)
 C[1,:] = [:Cone_cut Fx_opt FN_opt]
```

Cone with Paraboloidal Cap

```
### Definition of profile specific functions ###
function FN_cone_Rounded(b,d,E,x)
```

```
    t = acos(x)
    theta = atan((d*x/b)/((1-sin(t))/x+t))
    FN = E*(b/x)^2*tan(theta)*(t+4/3*(1-sin(t))/x+(1/3)*sin(t)*x)
end

function Fx_cone_Rounded(b,d,E,mu,x,s)
    v = acos(s)
    t = acos(x)
    theta = atan((d*x/b)/((1-sin(t))/x + t))
    Fx = (mu*E*tan(theta)) * (b/x)^2*(t+(4/3)
         *((1-sin(t))/x)+(1/3)*sin(t)*x - (4*(b/v)^3)/(3*b))
end

### Definition of objective and constraints ###
obj(b,x,s)= Fx_cone_Rounded(b,d,E,mu,x,s)
FN(b,x)= FN_cone_Rounded(b,d,E,x)

Cone_Rounded = Model(Ipopt.Optimizer)
register(Cone_Rounded, :obj, 3, obj; autodiff = true)
register(Cone_Rounded, :FN, 2, FN; autodiff = true)
@variable(Cone_Rounded, eps <= x <= 1 - eps)
@variable(Cone_Rounded, eps <= s <= 1 - eps)
@variable(Cone_Rounded, eps <= b <= 1)
@NLconstraint(Cone_Rounded, s <= (1-eps))
@NLconstraint(Cone_Rounded, x <= (1-eps))
@NLobjective(Cone_Rounded, Max, obj(b,x,s))
@NLconstraint(Cone_Rounded, FN(b,x)<=20)
optimize!(Cone_Rounded)
@show termination_status(Cone_Rounded)
@show primal_status(Cone_Rounded)
@show dual_status(Cone_Rounded)
@show objective_value(Cone_Rounded)

### Output definition of optimised parameters ###
b_opt,s_opt,x_opt = value(b),value(s),value(x)
a_opt = (b_opt/x_opt)
c_opt = (b_opt/s_opt)
FN_opt= FN(b_opt,x_opt)
Fx_opt = obj(b_opt,x_opt,s_opt)
theta_opt = atan((d*x_opt/b_opt)/((1-sin(acos(x_opt)))/x_opt + acos(x_opt)))*180/pi
R_opt = b_opt/((d*x_opt/b_opt)/((1-sin(acos(x_opt)))/x_opt + acos(x_opt)))

B = Array{Any}(undef,1,3)
B[1,:] = [:Cone_Rounded Fx_opt FN_opt]
```

Paraboloid

```
### Definition of profile specific functions ###
```

```
function FN_Paraboloid(d,E,G,a,mu,u0)
R = (a^2)/d
c = sqrt(a^2 - u0*G*R/(mu*E))
    FN = (4/3)*E*a^(3)/R
Fx = mu*FN*(1-c^3/a^3)
Fx,FN
end

### Definition of objective and constraints ###
obj(a)= FN_Paraboloid(d,E,G,a,mu,u0)[1]
FN(a)= FN_Paraboloid(d,E,G,a,mu,u0)[2]

Paraboloid = Model(Ipopt.Optimizer)
register(Paraboloid, :obj, 1, obj; autodiff = true)
register(Paraboloid, :FN, 1, FN; autodiff = true)
@variable(Paraboloid, 0 <= a <= 7) ### -> R>2
@NLobjective(Paraboloid, Max, obj(a))
@NLconstraint(Paraboloid, FN(a)<=20)
optimize!(Paraboloid)
@show termination_status(Paraboloid)
@show primal_status(Paraboloid)
@show dual_status(Paraboloid)
@show objective_value(Paraboloid)

### Output definition of optimised parameters ###
a_opt = value(a)
R_opt = (a_opt^2)/d
FN_opt= FN(a_opt)
Fx_opt = obj(a_opt)

C = Array{Any}(undef,1,3)
C[1,:] = [:Paraboloid Fx_opt FN_opt]
```

Truncated Paraboloid

```
### Definition of profile specific functions ###
function FN_Paraboloid_cut(E,a,s,d)
    FN = (2*E*d/3)*(1/a)*(3*a^2 - s)
end

function Fx_Paraboloid_cut(a,s,t,d,mu,E)
    Fx = (2*E*mu*d/3)*(1/a)*((3*a^2 - s) - (2*t - 3*s + 3*a^2)*sqrt(t/s))
end

### Definition of objective and constraints ###
obj(a,s,t)= Fx_Paraboloid_cut(a,s,t,d,mu,E)
FN(a,s)= FN_Paraboloid_cut(E,a,s,d)
```

```
Paraboloid_cut = Model(Ipopt.Optimizer)
register(Paraboloid_cut, :obj, 3, obj; autodiff = true)
register(Paraboloid_cut, :FN, 2, FN; autodiff = true)
@variable(Paraboloid_cut, eps <= a <= 5)
@variable(Paraboloid_cut, eps <= s <= (5-eps)^2)
@variable(Paraboloid_cut, eps <= t <= (5-eps)^2)
@NLconstraint(Paraboloid_cut, 0 <= t-s+a^2 <= 1-eps) #t-s+a^2 = c^2
@NLconstraint(Paraboloid_cut, 0 <= a^2 -s <= 1-eps) #a^2 -s = b^2
@NLconstraint(Paraboloid_cut, 1-(u0*G)/(mu*E) == (1/a)*(t/s)^(1/2))
@NLobjective(Paraboloid_cut, Max, obj(a,s,t))
@NLconstraint(Paraboloid_cut, FN(a,s) <= 20)
optimize!(Paraboloid_cut)
@show termination_status(Paraboloid_cut)
@show primal_status(Paraboloid_cut)
@show dual_status(Paraboloid_cut)
@show objective_value(Paraboloid_cut)

### Output definition of optimised parameters ###
a_opt,s_opt,t_opt = value(a),value(s),value(t)
FN_opt= FN(a_opt,s_opt)
Fx_opt = obj(a_opt,s_opt,t_opt)
R_opt = a_opt/d*s_opt
b_opt = sqrt(a_opt^2 - s_opt)
c_opt = sqrt(t_opt-b_opt^2)

B = Array{Any}(undef,1,3)
B[1,:] = [:Paraboloid_cut Fx_opt FN_opt]
```